Biomaterials 216 (2019) 119228

Contents lists available at ScienceDirect

Biomaterials

journal homepage: www.elsevier.com/locate/biomaterials

MR and PET-CT monitoring of tissue-engineered vascular grafts in the ovine carotid artery

Frederic Wolf[a], Vera Paefgen[b], Oliver Winz[c], Marianne Mertens[b], Sabine Koch[a], Nicolas Gross-Weege[b], Agnieszka Morgenroth[c], Anne Rix[b], Heike Schnoering[d], Khaled Chalabi[e], Stefan Jockenhoevel[a,**], Twan Lammers[b,f], Felix Mottaghy[c,g,1], Fabian Kiessling[b,1], Petra Mela[a,*,1]

[a] Dept. of Biohybrid & Medical Textiles (BioTex), Institute of Applied Medical Engineering (AME), Helmholtz Institute Aachen and Institute for Textiles Engineering (ITA), RWTH Aachen University, Forckenbeckstr. 55, 52074, Aachen, Germany
[b] Institute for Experimental Molecular Imaging, RWTH Aachen University Clinic, Forckenbeckstr. 55, 52074 Aachen, Germany
[c] Department of Nuclear Medicine, University Hospital RWTH Aachen, 52074, Pauwelsstr. 30, 52074 Aachen, Germany
[d] Clinic for Thoracic and Cardiovascular Surgery, University Hospital Aachen, Pauwelsstr. 30, 52074 Aachen, Germany
[e] Institut National de Chirurgie Cardiaque et de Cardiologie Interventionnelle, 2A, rue Nicolas Ernest Barblé, 1210 Luxembourg, Luxembourg
[f] Department of Targeted Therapeutics, University of Twente, PO Box 217, 7500 AE Enschede, the Netherlands
[g] Department of Radiology and Nuclear Medicine, Maastricht University Medical Center (MUMC+), P.O. Box 5800, 6202 AZ Maastricht, the Netherlands

ARTICLE INFO

Keywords:
Tissue-engineered vascular graft
Non-invasive monitoring
Multimodal monitoring
MRI
PET-CT
USPIO

ABSTRACT

The modification of biomaterials to comply with clinically employed monitoring techniques is a promising strategy to support clinical translation in regenerative medicine. Here, multimodal imaging of tissue-engineered vascular grafts (TEVG) was enabled by functionalizing the textile scaffold with ultrasmall superparamagnetic iron oxide (USPIO) nanoparticles. The resulting MR-imageable grafts (iTEVG) were monitored non-invasively throughout their whole life-cycle, from initial quality control to longitudinal functional evaluation in an ovine model for up to 8 weeks. Crucial features such as the complete embedding of the textile mesh in the developing tissue and the grafts' structural stability were assessed *in vitro* using 1T-, 3T- and 7T-MRI scanners. *In vivo*, the grafts were imaged by 3T-MRI and PET-CT. Contrary to unlabeled constructs, iTEVG could be delineated from native arteries and precisely localized by MRI. USPIO labeling neither induced calcifications, nor negatively affected their remodeling with respect to tissue-specific extracellular matrix composition and endothelialization. Functionality was confirmed by MR-angiography. ^{18}F-FDG uptake (assessed via PET-CT) indicated only transient post-surgical inflammation. In conclusion, USPIO-labeling enables accurate localization of TEVG and opens up opportunities for multimodal imaging approaches to assess transplant acceptance and function. Thereby, it can support clinical decision-making on the need for further pharmacological or surgical interventions.

1. Introduction

Tissue engineering aims at solving unmet clinical needs by developing tissue and organs biologically and mechanically equivalent to the healthy native ones. To this end, different paradigms have been proposed with the ultimate common endpoint of obtaining autologous living substitutes produced by the patient's own cells, endowed with the potential of growth and remodeling [1–4]. The advancements in the field of tissue engineering over the past decade have been tremendous [5], resulting in a continuously growing number of preclinical studies and in pilot clinical trials [6–12].

To enable a broad clinical translation of tissue-engineered constructs a concerted effort among academia, industry and certified bodies is needed to foster convergence between scientific progress and advancements in clinical, logistic and regulatory strategies. A fundamental aspect of this multifaceted challenge is the capability of non-destructively monitoring the implants at the fabrication stage and after implantation, to achieve pre-implantation *in vitro* quality assessment as well as longitudinal evaluation of the *in vivo* performance.

To a certain degree non-invasive monitoring of implants can be

* Corresponding author. Department of Biohybrid & Medical Textiles (BioTex), Institute of Applied Medical Engineering (AME), Helmholtz Institute Aachen, RWTH Aachen University, Forckenbeckstr. 55, 52074, Aachen, Germany..
** Corresponding author. .
E-mail addresses: jockenhoevel@ame.rwth-aachen.de (S. Jockenhoevel), mela@ame.rwth-aachen.de (P. Mela).
[1] equal contribution.

https://doi.org/10.1016/j.biomaterials.2019.119228
Received 11 December 2018; Received in revised form 16 May 2019; Accepted 25 May 2019
Available online 27 May 2019
0142-9612/

performed with imaging technologies that are already routinely used in the clinic [13,14]. This has the advantage of a faster clinical entry by avoiding time-consuming validation and approval, and usually having a faster acceptance by the clinicians. In this respect, particularly ultrasound, computed tomography (CT) and magnetic resonance imaging (MRI) have been explored to advance the development of tissue-engineered cardiovascular implants. Specifically, ultrasound has been shown to be a valuable tool to monitor changes in extracellular matrix production *in vitro* over time [15–18]. The application of different ultrasound modes to bioreactors for heart valves and vascular grafts [19,20] provided information on the 3D geometry otherwise not accessible by conventional optical imaging as well as visualization and quantitative evaluation of the flow through the construct, in real time and throughout the entire *in vitro* fabrication phase.

CT-imaging was used to follow non-invasively the degradation of non-cellularized synthetic vascular grafts developed for in situ tissue engineering by Talacua et al. using polycaprolactone modified with a novel iodinated CT contrast agent. The authors were able to measure the volume and density of the graft and to assign the decrease in density on CT images to the scaffold degradation [21].

Another widely clinically applied technique for non-invasive assessment of the function and structure of the cardiovascular system is MRI. MRI certainly offers the best soft tissue contrast of all imaging modalities and a broad variety of tools to characterize tissues functionally. MRI was, for example used to assess wall shear stress in tissue-engineered vascular grafts [22]. Nevertheless, due to very similar soft tissue properties of tissue-engineered constructs and native tissues, contrast agents, such as ultrasmall superparamagnetic iron oxide (USPIO) nanoparticles, 19F-containing compounds and gadolinium-based complexes, often need to be incorporated to enable a proper delineation of the implanted material [23–27]. USPIO particles have been proposed for a wide range of applications including stem cells tracking, cancer detection and drug delivery monitoring [28–31]. For cardiovascular tissue engineering applications, aortic smooth muscle cells (SMC) [32] and endothelial cells (EC) [33,34] were labeled with USPIO to enable a non-invasive monitoring of tissue-engineered vascular grafts within a clinically relevant time-window to assess eventual endothelial damage after implantation.

Towards our goal of bringing biohybrid tissue-engineered vascular grafts to the clinic, we established the technology and experimental procedures to make them MRI-imageable to enable a clear delineation of the grafts during the bioreactor cultivation and showed proof-of-principle visualization of a USPIO-labeled graft implanted as arteriovenous shunt in adult sheep [35]. In this study, we built on our previous efforts and further expanded the monitoring scheme with positron emission tomography-computed tomography (PET-CT) using fluordeoxyglucose (FDG) as a metabolic tracer [36] to monitor the whole life-cycle of tissue-engineered vascular grafts non-invasively, starting from *in vitro* quality control assessment to multimodal longitudinal evaluation of the grafts' functionality for up to eight weeks in an ovine model. We combined data provided by MRI to monitor the grafts' localization and function, with data obtained by FDG PET-CT to identify and eventually accurately quantify vascular inflammation. Biohybrid grafts were fabricated with textile co-scaffolds labeled with USPIO (iTEVG) and without any labeling (TEVG). Upon explantation, the grafts were examined to evaluate the influence of the USPIO labeling on the tissue formation. Analyses included immunohistochemistry, quantification of collagen content and burst strength determination. The presence of the USPIO clearly increased the detectability of the vascular grafts by MRI enabling their precise localization without significantly affecting the extracellular matrix synthesis.

2. Materials and methods

The study design is schematically shown in Fig. 1. Autologous tissue-engineered vascular grafts were prepared by a molding technique using cells isolated from the ovine carotid arteries, fibrin gel components and USPIO-labeled (iTEVG, n = 6) or non-labeled (TEVG, n = 6) textile meshes. The grafts were dynamically conditioned *in vitro* over two weeks. Three grafts of each kind were implanted as carotid artery interponates in the respective sheep for up to 8 weeks, while the remaining grafts were used for tissue analysis. Prior to implantation the TEVG and iTEVG were visualized by 3T MRI for quality assessment. The implants were followed up longitudinally by MRI at weeks 4 and 8, as well as by PET-CT at weeks 1 and 3. After explantation, the tissue were analyzed (immuno)histochemically and biochemically to evaluate tissue composition and endothelialization.

A further set of grafts was prepared exclusively for MRI *in vitro* characterization using different magnetic field strength MR systems (1, 3 and 7T) to investigate the feasibility to quantitatively evaluate relaxometric properties and assess the proper embedding of the textile mesh in the tissue as quality control.

The animal experiment was approved by the governmental review committee on animal care (84-02.04.2012.A351). Six healthy adult sheep (Rhoen sheep or Rhoen sheep mixed breed) were used, for the evaluation of three TEVG and three iTEVG. The animals were enrolled from a disease-free barrier breeding facility, were housed in ventilated rooms and allowed to acclimatize to their surroundings for a minimum of five days before surgery. Animals were fasted overnight before the surgical procedure, with water allowed ad libitum.

2.1. Carotid artery harvest

After premedication with intramuscular atropine 1% (0.1–0.15 mg/kg) and xylazine 2% (0.15–0.2 mg/kg), a two-lumen central venous line was inserted in the left jugular vein. Propofol (3–4 mg/kg) was administered and endotracheal intubation was performed. The animal was placed in the left lateral position. Anesthesia was maintained with isoflurane (1.5 vol%) and fentanyl (45–90 mg/kg/h). The operative field was prepped and dressed. The right common carotid artery and jugular vein were dissected over a length of approximately 10 cm. A bolus of heparin (5000 U) was administered via the central line. A 6 cm segment of the right common carotid artery was harvested from each animal and immediately placed in sterile transport buffer (100 mM HEPES, 140 mM NaCl, 2.5 mM KCl, 10 mM glucose, 1% antibiotic/antimycotic solution (penicillin G/streptomycin/amphotericin B; Gibco, Karlsruhe, Germany); pH 7.4). Continuity of the carotid artery was re-established with a thin-walled 6-mm diameter GORE-TEX® graft (W.L. Gore & Associates, Newark, Delaware, USA), which was sewn in place using running 6-0 polypropylene (Prolene®, Ethicon, Somerville, New Jersey, USA). After careful hemostasis, the wound was closed in layers. The administration of narcotic agents was discontinued. The animals were extubated within 30 min. Subsequently, the central venous line was removed and the animals were transferred to the adjacent observation barn for the next 48 h. Thereafter, the animals were transferred to the institute farm until the graft implantation procedure.

2.2. Cell isolation and culture

Ovine carotid artery endothelial cell (EC) and smooth muscle cell (SMC)/fibroblast (FB) isolation was performed as described previously [37]. The carotid artery biopsy was washed with PBS, cannulated on both ends and EC were obtained by collagenase type I treatment for 30 min at 37 °C. The artery was carefully flushed with PBS to collect EC, which were then seeded on gelatin pre-coated culture flasks. A SMC/FB mixture was isolated by cutting 1 mm thick tissue rings and placing them in cell culture flasks. Outgrowing cells were observed after one week. EC were kept in endothelial basal medium (EBM-2) supplemented with endothelial growth supplements (EGM-2) (Lonza, Cologne, Germany). SMC/FB were cultured in DMEM supplemented with 10% fetal calf serum (FCS) (Life Technologies, Karlsruhe, Germany).

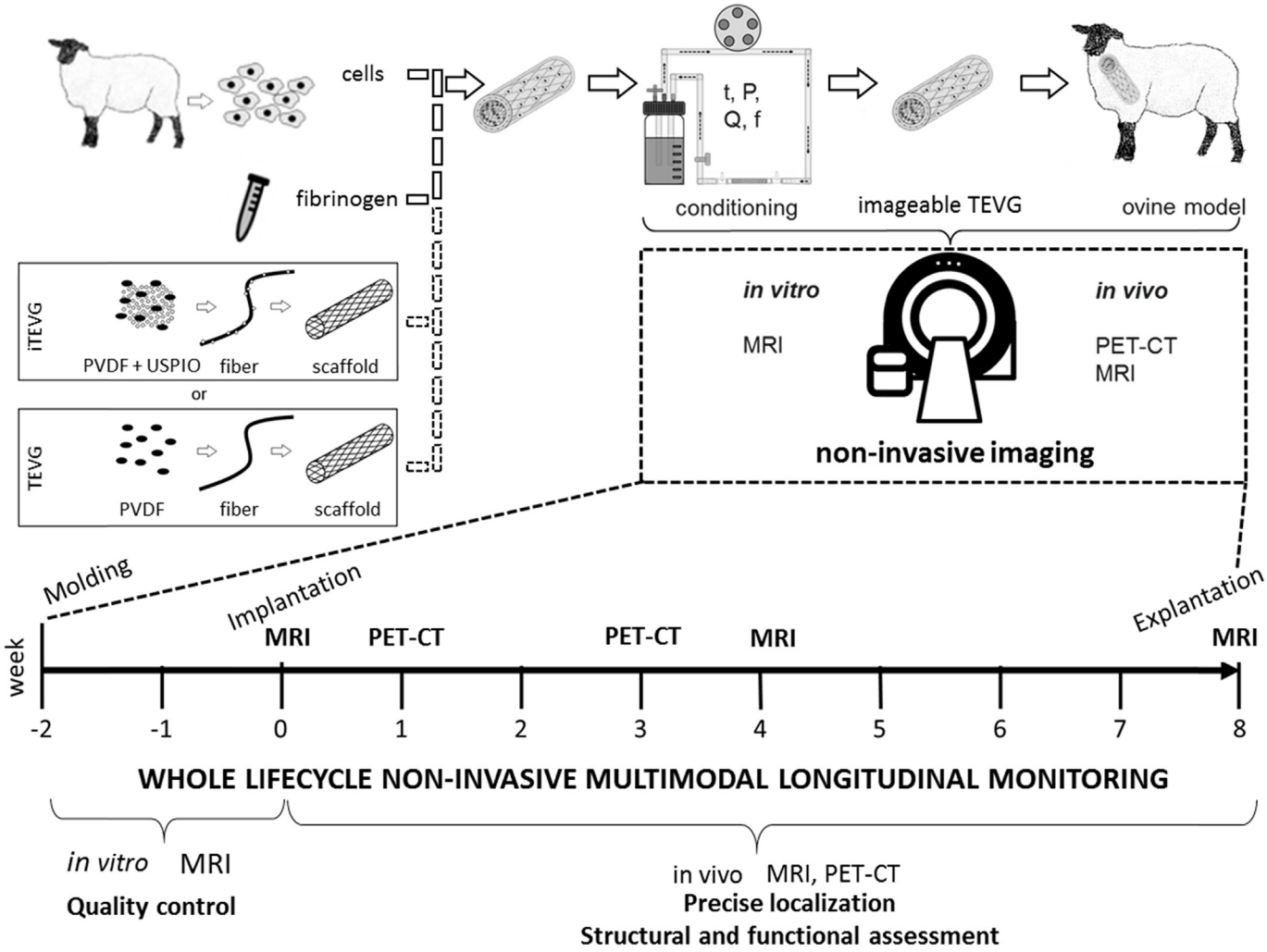

Fig. 1. Study design. Schematic representation of the fabrication process for imageable USPIO-labeled and non-labeled (TEVG) tissue-engineered vascular grafts (iTEVG) and experimental timeline for *in vitro* and *in vivo* graft monitoring.

Cells were subcultured at a confluency of 80–90%. EC between passage 3 and 5 and SMC/FB between passage 4 and 6 were used to fabricate tissue-engineered vascular grafts (TEVG) and imageable tissue-engineered vascular grafts (iTEVG) for the *in vitro* and *in vivo* experiments. Before experiments were conducted, their cellular phenotypes were verified by immunohistochemical staining against alpha-smooth muscle actin (α-SMA) and von Willebrand factor (vWf). SMC/FB had to be positive for α-SMA and negative for vWF, EC had to show the opposite results. Cells were seeded in 96-well plates, fixed with ice-cold methanol (−20 °C) for 30 min and rehydrated in PBS. Subsequently, blocking of unspecific epitopes and permeabilization of the cell membranes was performed with normal goat serum (NGS; Dako, Hamburg, Germany) in 0.1% Triton-PBS for 1 h. Cells were incubated for 1 h at 37 °C with the following primary antibodies: 1:400 mouse anti-a-SMA (A 2547; Sigma, Steinheim, Germany) and 1:200 rabbit polyclonal anti-human vWf (A0082; Dako). Secondary antibodies were incubated for 1 h at 37 °C: 1:400 mouse immunoglobulin G (H + L) (A 11005; Invitrogen) and 1:400 rabbit immunoglobulin G (H + L) (A11008; Invitrogen). The cells were counterstained with DAPI nucleic acid stain (Molecular Probes) and visualized using a microscope capable of epi-illumination (AxioObserver Z1; Carl Zeiss GmbH). Images were acquired using a digital camera (AxioCam MRm; Carl Zeiss GmbH).

2.3. Fibrin synthesis

Lyophilized human fibrinogen (Calbiochem®, Darmstadt, Germany) was dissolved in purified water (Milli-Q™; Millipore, Schwalbach, Germany) and dialyzed with a cut-off membrane (Novodirect, Kehl, Germany) of 6000–8000 MW overnight against tris-buffered saline (TBS; pH 7.4). Subsequently, the fibrinogen solution was sterilized by filtration (0.22 µm filter) and the concentration was optically determined by absorbance measurement at 280 nm using a spectrophotometer (Tecan, Crailsheim, Germany). The fibrin gel component of the vascular graft (5.0 mL in total) consisted of 2.5 mL of the fibrinogen solution (10 mg/mL), and the fibrin polymerization starting solution composed of 1.75 mL TBS containing 50×10^6 carotid artery SMC/FB, 0.375 mL 50 mM $CaCl_2$ (Sigma, Steinheim, Germany) in TBS and 0.375 mL of thrombin (40 U/mL; Sigma, Steinheim, Germany).

2.4. USPIO synthesis and USPIO-labeled PVDF mesh production

USPIO-labeled PVDF warp-knitted mesh was fabricated as previously described [35]. USPIO nanoparticles were synthesized by co-precipitation of ferrous (Fe^{2+}) and ferric (Fe^{3+}) salts under alkaline aqueous conditions following a modified one-pot synthetic protocol, which was published previously [38]. The resulting USPIO are known to have a diameter of 5.5 ± 1.1 nm as determined by transmission electron microscopy [38]. Lyophilized USPIO particles (0.2% (w/w))

and PVDF granules (Solef®1006 by Solvay Solexis S.A.S., Tavaux, France) were mixed in a rotatory mixing station (Stuart rotator drive STR4, Bibby Scientific Ltd, United Kingdom) and subsequently processed to fibers via melt-spinning using a single-screw lab-melt-spinning machine (Fourné Polymertechnik GmbH, Germany). The fibers were further processed into tubular warp-knitted structures on a double Raschel warp-knitting machine (DDR 16 EAC/EEC, Karl Mayer Textilmaschinenfabrik GmbH, Obertshausen, Germany). Fibers obtained with (n = 35) and without USPIO (n = 35) were analyzed by means of a digital microscope (Keyence VHX 5000) to determine their diameter, which was 20 ± 2 µm for both types.

2.5. Tissue-engineered vascular grafts fabrication and bioreactor conditioning

Biohybrid vascular grafts were fabricated by injection molding with a procedure adapted from a previously reported one [37]. Briefly, the inner casting cylinder of the mold was either lined with the non-labeled or USPIO-labeled PVDF mesh which was fixed in-between of two T-connectors. Subsequently, the annular space between the inner (O.D. 5 mm) and outer (I.D. 8 mm) cylinders of the mold was filled with the fibrin gel components. The fast polymerization of the fibrinogen provided a homogenous cell distribution throughout the graft. The inner casting cylinder was removed after 45 min and the graft was maintained in the outer cylinder. Subsequently, the graft in the outer cylinder was directly connected to a bioreactor system and transferred to an incubator at 37 °C and 5% CO_2 for dynamic conditioning. The flow through the grafts was generated by a peristaltic pump (MCP-Process; Ismatec) and was gradually increased from 20 to 200 mL/min in 30 mL/min daily steps over a 7-day period. A flow resistance positioned distal to the graft enabled the regulation of pressure to arterial levels (120 mmHg, systolic pressure; 80 mmHg, diastolic pressure). The pressure was monitored proximal to the graft by a pressure sensor (Codan Medical GmbH), and recorded by a computer via an analog/digital converter (USB6009; National Instruments). The bioreactor tubing was composed of platinum-cured silicone peroxide (Ismatec), with high gas transfer coefficients for both oxygen and carbon dioxide to provide stable culture conditions.

After 7 days the graft in the outer cylinder was removed from the bioreactor system for endothelialization of the graft's lumen. 3×10^6 cells/mL were injected into the lumen and the graft was rotated around its longitudinal axis at 1 round per minute for 6h to guarantee homogenous EC attachment. Afterwards, the graft was reconnected to the bioreactor system and conditioned for 7 more days following the same protocol as in the first week. The culture medium used in the bioreactor system for the first 7 days consisted of DMEM with 10% FCS, 1% antibiotic/antimycotic solution (ABM), 1.6 µL/mL tranexamic acid (TA) (Cyklokapron- Injection solution 1000 mg/mL; Pfizer Pharma GmbH) and L-ascorbic acid-2-phosphate (1.0 mM; Sigma). After EC seeding, the medium was replaced by a 50:50 (v/v) mixture of DMEM and EGM-2 supplemented with 10% FCS, 1% ABM, 1.6 mL/mL TA and L-ascorbic acid-2-phosphate.

2.6. Implantation of tissue-engineered vascular grafts

Following bioreactor conditioning, tissue-engineered vascular grafts were implanted into the carotid artery of the same animals (n = 6) from which the cells had been harvested. Each animal was placed in the right lateral position, and the operative field was prepped and dressed. The grafts were removed from the bioreactor within the operating theatre and prepped for surgery. For implantation of the grafts, 4–5 cm of native left common carotid artery was excised, and a 4–5 cm section of the tissue-engineered graft was sewn in place end-to-end, completing the distal and proximal anastomoses using running 6-0 polypropylene. Subsequently, the wound was closed and animals were transferred to the observation barn the following morning.

2.7. Explantation of tissue-engineered vascular composite grafts

The vascular composite grafts were explanted at the predetermined end points of eight weeks. At the scheduled end of the experiment, the animals were euthanized with pentobarbital (50–80 mg/kg; Marial GmbH, Hallbergmoos, Germany). After explantation the grafts were rinsed with PBS, carved longitudinally and inspected for thrombotic deposits. After photo documentation, representative portions of the explanted grafts were fixed in Carnoy's fixative for (immuno)histological analysis or were processed for hydroxyproline assay.

2.8. Tissue analysis of tissue engineered vascular grafts

2.8.1. Immunohistochemistry

Non-specific sites on Carnoy's fixed, paraffin-embedded graft sections were blocked with 5% normal goat serum (NGS; Dako) in 0.1% Triton-PBS for 1 h at room temperature (RT). Subsequently, sections were incubated for 1 h at 37 °C with the following primary antibodies: 1:200 rabbit anti-type collagen I (R 1038; Acris); 1:25 rabbit anti-type collagen III (R 1040; Acris); 1:200 rabbit anti-elastin (20R- ER003; Fitzgerald); and 1:1000 mouse anti-a-SMA (A 2547; Sigma).

Afterwards, the sections were incubated for 1 h at 37 °C with either rhodamine or fluorescein-conjugated goat anti-mouse or goat anti-rabbit secondary antibodies: 1:400 rabbit type collagen I (A 11008; Molecular Probes); 1:300 rabbit type collagen III (E 0432; Dako); 1:400 rabbit elastin (A 11008; Molecular Probes); and 1:400 mouse a-SMA (A 11005; Molecular Probes). Type collagen III signal was amplified by an additional incubation with 1:1000 streptavidin/TRITC (RA 021; Acris). The native ovine carotid arteries served as positive controls. As negative controls, samples were incubated in diluent with the secondary antibody only. Tissue sections were counterstained with DAPI nucleic acid stain (Molecular Probes). Additional negative controls were obtained by staining for markers not specific for vascular tissue as explained in the Supplementary Information. Samples were investigated with a microscope equipped for epi-illumination (AxioObserver Z1; Carl Zeiss GmbH). Images were acquired using a digital camera (AxioCam MRm; Carl Zeiss GmbH).

2.8.2. Mechanical properties

Burst pressure experiments were performed by fixing a piece of each vascular graft (1 cm^2) onto a custom-designed burst chamber and exposing it to increasing pressure by pumping PBS into the chamber by means of a peristaltic pump. The tissue was placed on the outlet of the chamber and was fixed by the chamber's lid. To avoid leakage and tissue damage by sharp edges two rubber gaskets were used to sandwich the sample. The pressure was recorded by a pressure sensor device (Jumo Midas pressure transmitter; JUMO GmbH & Co. KG) connected to a computer running LabVIEW 7.1 (National Instruments Corporation). The highest pressure measured before the point of structural failure was recorded as the burst strength of the graft.

2.8.3. Quantification of collagen content (hydroxyproline assay)

For the quantitative analysis of collagen synthesis, the hydroxyproline content of overnight vacuum dried samples from each vascular graft was determined as described by Reddy and Enwemeka [39]. After the samples were hydrolyzed by addition of 6 M HCl and heat treatment (18 h at 110 °C), buffered Chloramine-T reagent (60 mM Chloramine-T, 20% n-Propanol, 80% Acetate citrate buffer) was added to oxidize the samples for 45 min. Ehrlich's reagent (4-dimethylaminobenzaldehyde, Fluka) was subsequently added and the samples were incubated for 45 min at 65 °C. After the development of a red condensation product, the absorbance was measured at 550 nm with a Tecan plate reader (Infinite M200, Tecan Group Ltd.). A standard curve of known amounts of *trans*-4-hydroxy-L-proline (Sigma) was used for calibration and to quantify the results. Results are expressed as percentage of the collagen amount of the native ovine carotid artery.

2.9. Magnetic resonance imaging in vitro

The vascular grafts to be implanted were measured in a clinical 3T whole-body MR scanner (Philips Achieva, Best, The Netherlands) using a custom-made small animal solenoid sense-receive coil (40 mm inner diameter and 78 mm bore length; resulting in a 40 mm field of view) (Philips Research Laboratories, Hamburg, Germany) for reception of the signal together with the body coil for excitation. For the quality control of the implants, the bioreactor circuit with the grafts was uncoupled from the pump, transferred into the MR scanner, and measurements were performed at the end of the cultivation phase, as close as possible to the time of implantation. Transverse (T2) relaxation times were measured in 2D scan mode using a multi-slice, multi-shot spin-echo sequence (MSME) with a 90° excitation pulse followed by a train of equally spaced 180° refocusing pulses [TR = 1500 ms, echo time (TE) = 29 ms, number of echoes = 20, reconstruction matrix = 112 × 112, voxel size = 0.2 × 0.2 mm, slice thickness = 1 mm]. For T2* relaxometry, images at 32 echo times [TE range = 14–168 ms] were acquired by using a multi-shot, multi-slice fast-field gradient-echo sequence [TR = 549 ms, 11 ms interval between two echoes, reconstruction matrix = 192 × 192, voxel size = 0.25 × 0.25 mm, slice thickness = 1 mm, 30° flip angle]. T2 and T2* relaxation times (and corresponding R2 and R2* ratios) were calculated by fitting an exponential curve to the signal amplitudes as a function of TE for each segmented scaffold region using the Imalytics Preclinical Software (Gremse-IT GmbH, Aachen, Germany) [40]. The exponential curve includes an offset to account for a signal plateau created by noise or a component with slow signal decay. Furthermore, T1- and T2-weighted images were acquired using a T1-weighted turbo-spin-echo (TSE) sequence [TR = 500 ms, TE = 20 ms, 0.30 × 0.23 mm voxel size, slice thickness = 1 mm], and a T2-weighted TSE sequence [TR = 1000 ms, TE = 100 ms, 0.25 × 0.25 mm voxel size, slice thickness = 1 mm], whereas for PD-weighting, a multi-shot, multi-slice fast-field gradient-echo (FFE) sequence [TE = 4 ms, TR = 1000 ms, FA = 60°, voxel size = 0.25 × 0.25 mm, slice thickness = 1 mm] was used.

An additional set of vascular grafts (iTEVG,n = 1 and TEVG, n = 1) was exclusively evaluated *in vitro* with preclinical MRI scanners with 1T, 3T and 7T field strengths (Bruker, Ettlingen, Germany; 1T Icon and the 7T Biospec 70/20 USR) at different locations along their axes (n ≥ 3). These grafts were prepared as described in section 2.5, however they were produced with a smaller diameter (3 mm inner diameter instead of 5 mm as for the animal study) and with human smooth muscle cells and endothelial cells isolated from umbilical arteries. Furthermore, for these grafts, the bioreactor system was driven by a microcentrifugal pump instead of a peristaltic one. For the 1T measurements, a rat whole body volume coil (59/50 × 90 mm) was used. T2-weighted scans at the 1T MRI were acquired by using a RARE (rapid imaging with refocused echos) sequence [TR = 1600 ms, TE = 80 ms, RARE factor = 8, averages = 6, matrix = 128 × 128, voxel size = 0.125 × 0.125 × 1 mm]. For 7T T2w images, a TurboRARE sequence was used [TR = 2500 ms, TE = 48 ms, RARE factor = 8, averages = 4, matrix = 128 × 128, voxel size = 0.101 × 0.101 × 1 mm]. T2*-weighted images were generated using a FLASH sequence [TR = 800, TE = 30 ms, FA = 18°]. For R2 determination, a MSME sequence [TR = 3000 ms, TE = 20, number of echos = 30], and for R2* determination a MGE (multiple gradient echo) sequence with TR = 800 ms and TE = 4.5 ms [number of echos = 8, averages = 2, FA = 50°] were applied. All 7T scans were obtained at identical matrix size and resolution, using two different coil configurations: the 3D images were acquired with the volume transmit/receive coil (86 mm inner diameter; Bruker RF RES 300 1H 112/086 QSN TO AD); all other measurements were performed with a planar surface coil for signal reception (20 mm inner diameter; Bruker RF SUC 300 1H LNA AV3) in combination with the volume coil for transmission. T2 and T2* relaxation times (and corresponding R2 and R2* ratios) were calculated as described for 3T-MRI. The regions of interest (ROIs) were defined as explained in Figs. S1 and S2.

2.10. In vivo longitudinal monitoring

The implanted grafts were longitudinally monitored by MRI and FDG PET-CT for a period of 2 months (Fig. 1). FDG PET-CT imaging was used to monitor inflammation 1 and 3 weeks post-implantation, MR imaging was performed to visualize the biohybrid vascular grafts' localization and functionality, as well as the textile-reinforcement integrity at 4 and 8 weeks post-implantation.

2.10.1. MRI

MR imaging of the implanted grafts was carried out under Xylazin/Atropin anesthesia using a clinical 3T MR scanner, in combination with PMS SENSE Head Spine Coil (Philips Research Laboratories, Hamburg, Germany). Grafts were visualized using a proton-weighted multi-shot, multi-slice fast-field gradient-echo (FFE) sequence [TE = 4 ms, TR = 1000 ms, FA = 60°, FOV = 60 × 22 × 60 mm], and patency was evaluated using a 3D T1-weighted FFE phase contrast angiography (PCA) [TE = 4 ms, TR = 10 ms, FA = 15°, averages = 2, FOV = 68 × 300 × 150 mm, matrix = 512 × 265]. For *in vivo* R2 determination, a turbo spin echo (TSE) sequence [TR = 1500 ms, TE = 18.6–241.2 ms, FA = 90°, averages = 2, matrix size 80 × 80, resolution = 0.96 × 0.96 × 1 mm] was used. Scans for R2* determination were obtained using a FFE sequence [TR = 200 ms, TE = 1.8–14.2 ms, FA = 30°, matrix = 112 × 112, averages = 10 resolution 0.86 × 0.86 × 2 mm]. As for the *in vitro* studies, T2 and T2* relaxation times (and corresponding R2 and R2* ratios) were calculated by fitting an exponential curve to the signal amplitudes as a function of TE for each segmented scaffold region using the Imalytics Preclinical Software (Gremse-IT GmbH, Aachen, Germany). Reliable evaluation was possible for all but one iTEVG for which R2 could not be determined for the 4 week time point because of insufficient scan quality and for one animal with a TEVG, which was euthanized at week 4 as explained in section 3.2.

2.10.2. PET-CT

Imaging was performed on a Gemini TF 16 PET/CT scanner (Philips Medical Systems, Best, The Netherlands) which consists of a 16-slice Brilliance CT scanner and a fully three-dimensional, time-of-flight (TOF) capable PET scanner. The PET scanner is constructed with 28 flat modules, each consisting of a 23 × 44 array of 4 × 4x22 mm lutetium-yttriumoxyorthosilicate (LYSO) crystals placed in a full ring. The scanner bore has a diameter of 71.7 cm with active transverse and axial field of views (FOV) of 57.6 and 18 cm, respectively for both the PET and the CT component.

All animals were measured twice except one that was measured four times. All animals received at least 2 MBq ^{18}F-FDG/kg body weight (324 ± 44 MBq ^{18}F-FDG, range: 275–413 MBq). First a whole body low-dose CT was performed without contrast medium for attenuation correction purposes (scanning parameters: collimation 16 × 1.5 mm; pitch 0.812; rotation time 0.4 s; effective tube current–time product of 30 mAs; tube voltage of 120 kVp). Following the low-dose CT, a contrast-enhanced (300 mg/mL, Ultravist 300; Bayer Schering Pharma) arterial CT scan was performed by scanning the neck from the base of the skull to the upper thorax. Subsequently, the venous phase was measured for the whole body. Images were reconstructed with a slice thickness of 5 mm at overlapping increments of 3.5 mm, resulting in a CT voxel size of 1.2 × 1.2 × 3.5 mm^3. The image reconstruction algorithm was a medium smooth soft-tissue kernel (windows center, 60; windows wideness, 450). The static PET scan started 60 min after the intravenous injection of ^{18}F-FDG with an acquisition time of 1.5 min per bed position. Data were collected in list mode for all coincident events along with their time stamps. For each animal, 14 to 17 bed positions were acquired. PET slices of 4 mm thickness (pixel size 4 × 4 mm) were

reconstructed using the proprietary iterative BLOB–OS–TF algorithm (number of iterations = 3, number of subsets = 33) which is provided by the scanner's manufacturer. This results in a matrix size of 144 × 144 voxels per slice. A full correction for random coincidences, scatter radiation, and attenuation was performed. Attenuation correction of PET data was based on the low-dose unenhanced CT data.

Quantitative analysis was performed with the PMOD 3.1 software package (PMOD Technologies Ltd, Zurich, Switzerland). Mean and maximum standard uptake values (SUVmean and SUVmax, respectively) were measured in seven different defined regions of interest (Fig. S2): left common carotid artery including implant, right common carotid artery including GORE-TEX® implant, right and left jugular vein, caudal part of left and right carotid artery and thigh muscle of the right foreleg (reference region). All ROI were defined on the arterial and venous contrast-enhanced CT scans and transferred to the co-registered static PET scans.

2.11. Statistical analysis

All results are presented as average ± standard deviation. For comparison of burst pressures and hydroxyproline contents, one-way ANOVA was performed; for comparisons of R2, R2*(MRI), SUV (PET) paired *t*-test was performed when different time points (for the same animal) were analyzed, otherwise one-way ANOVA was performed.

For the *in vitro* evaluation of R2 and R2* a two way ANOVA was performed to take into account the effect of USPIO presence and field strength, while paired *t*-test was chosen to account for the effect of time. When statistically significant differences were detected between group means ($n > 2$) Bonferroni post-hoc test was performed for pair wise comparisons. $P \leq 0.05$ was considered as significant. Analysis was performed using SPSS (version 24.0, IBM, USA).

3. Results and discussion

3.1. In vitro characterization of the tissue-engineered vascular grafts

For each sheep either two TEVG or two iTEVG were fabricated by injection molding of cell-containing fibrin followed by a two-week cultivation in a bioreactor. One of the grafts was used for the analysis of *in vitro* tissue development while the other one was implanted as carotid artery interponate to evaluate its *in vivo* performance.

Shortly before implantation, the tissue-engineered vascular grafts were imaged by 3T MRI, while enclosed in the bioreactor system, to evaluate their shape, patency, contrast properties and relaxation rates. The bioreactor system consists of silicone tubings for the circulation of the medium and the housing of the TEVG, which can be easily detached from the peristaltic pump and introduced into the MRI scanner, as done in this study.

USPIO incorporation resulted in enhanced visibility in T1-, T2*- and PD-weighted images (Fig. 2 B) and in a statistically significant increase in R2* (Fig. 2C) in a clinical 3T MRI system, confirming the reproducibility and efficiency of USPIO textile labeling for *in vitro* structural evaluation of the grafts [35]. The lumens of TEVG and iTEVG were open and the 3D rendering of the USPIO-labeled mesh (Fig. 2 D) did not reveal any signs of structural collapse. The complete embedding of the mesh within the thickness of the graft's wall could also be confirmed by MRI (Fig. 2 A). This is an important aspect in the quality control of the implant as direct exposure of the textile to the blood might cause thrombus formation. Such detailed evaluation could not be achieved with other non-invasive monitoring techniques. Ultrasound imaging has been applied to evaluate the overall structural integrity of TEVG *in vitro* [20], however to achieve higher spatial resolution, ultrasound transducers with high frequencies are needed. As these have low tissue penetration depths, their application in closed bioreactor systems under sterile conditions is challenging [41].

Another set of grafts (n(iTEVG) = 1, n(TEVG) = 1) was prepared exclusively for the evaluation *in vitro* at multiple locations along their axes ($n \geq 3$) with MRI scanners operating at 1T and 7T, besides the clinical 3T scanner. The 1T MRI imaging was employed and evaluated as an easy applicable low cost imaging method to control successful USPIO labelling and textile embedding in the graft. In all systems the grafts were detectable, with the iTEVG giving a higher contrast (Fig. 3 A). Evaluation of the graft embedding was feasible for iTEVG at 1T, although with a trade-off between scanning duration and resolution to avoid keeping the graft for a long time in the scanner under non-optimal conditions. The *in vitro* quality control is, therefore, feasible even in more basic MRI systems of tabletop size and without superconducting magnets. However, analysis of the grafts' relaxometric properties was only partially possible at 1T. While R2 quantification indicated a significant difference ($p < 0.05$) between USPIO-labeled ($R2 = 3.29 \pm 0.06\ s^{-1}$) and non-labeled TEVG ($R2 = 3.14 \pm 0.02\ s^{-1}$), R2* evaluation could not be properly performed in the 1T system because of field inhomogeneities of the permanent magnet.

For the 7T MRI, an additional quantitative analysis of R2 and R2* relaxation rates was performed over a cultivation period of 14 days and data were compared to those from 3T measurements. The R2 and R2* rates obtained with the 7T scanner were significantly higher than those at 3T for all grafts, with the values for iTEVG being almost 2.8 fold higher. As already seen in the previous 3T measurements, the R2 and R2* rates remained stable over time, with a significant difference between TEVG and iTEVG.

Fig. 3C shows a 3D rendering of an iTEVG after 7 days obtained in a 7T MRI system using the Imalytics Preclinical software, showing the same capability to evaluate the structural stability of the graft as for the 3T system, but with a higher resolution. A shorter scanning time is a further advantage of higher magnetic field systems such as the 7T MRI, however these systems are currently not broadly available in the clinic. Acquisition of T2-weighted images of the grafts with and without perfusion in the 7T scanner further showed patency of the grafts (Fig. 3 D). These measurements were enabled by the use of a portable bioreactor system we recently developed by implementing a centrifugal pump and an ad-hoc developed controller [42]. The system was meant to address logistic issues related to the transport of the tissue-engineered grafts so that they are constantly under physiological flow and pressure conditions to guarantee viability, stability and function prior to implantation. The T2-weighted images allow to evaluate the homogenous embedding of the USPIO particles into the mesh (Fig. S3) as well as the mesh position with respect to the graft's luminal side (Fig. S4).

Based on these findings, we conclude that benchtop 1T MRI scanners may suffice to confirm scaffold labelling during the production process. These devices are considerably cheap with respect to system's price and maintenance costs, can be used in a normal laboratory environment and they are easy to handle. High-field devices as the preclinical 7T MRI provide more quantitative and accurate results but are costly and may not always be required for characterizing the vascular scaffolds *in vitro*.

Tissue characterization included immunohistochemical stainings of different extracellular matrix (ECM) proteins, biochemical evaluation of the hydroxyproline content and measurement of the burst strength. Immunohistochemistry of iTEVG and TEVG prior to implantation confirmed the good integration of the textile reinforcement in the vessel wall. Stainings against collagen type I and type III showed deposition of ECM proteins after 14 days of bioreactor cultivation (Fig. 4A–F), with no detectable differences between iTEVG and TEVG. Furthermore, elastin synthesis was observed (Fig. 4G–I) and the embedded cells were positive for α-SMA in both types of tissue-engineered vascular grafts (Fig. 4J–L). Negative controls are shown in Figs. S5–S7. The amount of collagen, a main component of native vessels, of TEVG and iTEVG as calculated from the hydroxyproline content was not statistically different (Fig. 4 M). The burst strength, a common value to characterize the mechanical behavior of a tissue exposed to pressure, showed similar results for TEVG and iTEVG (Fig. 4 N) supporting the observation that

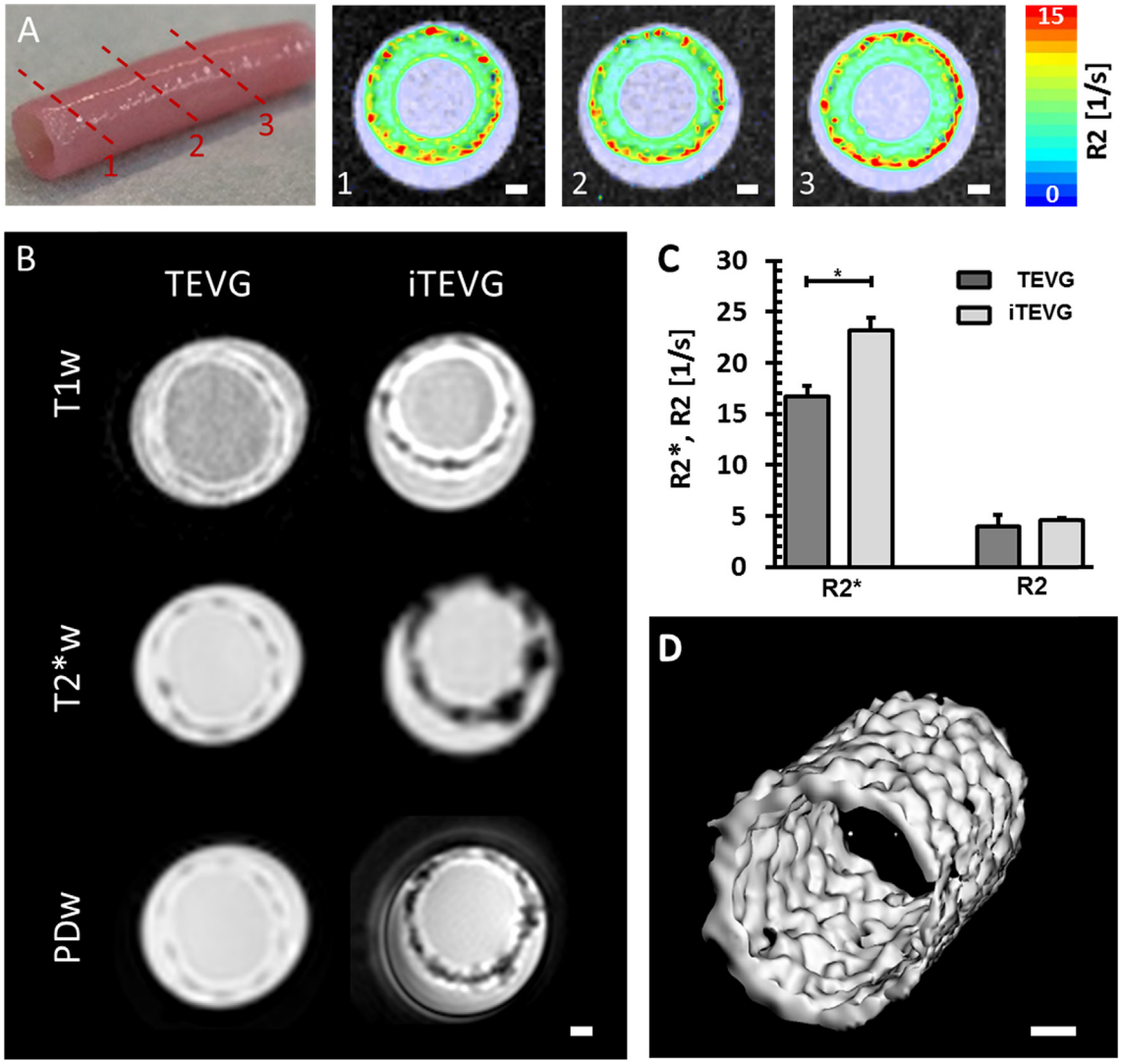

Fig. 2. 3T-MR characterization of TEVG (n = 3) and iTEVG (n = 3) prior to implantation. A) Photograph of an iTEVG after bioreactor conditioning (left) and MR relaxometry with R2 mappings at three different sections to demonstrate mesh embedding in the grafts (right, scale bar = 1 mm). In this context, the red dots in the R2 maps represent the USPIO in the mesh. B) Suitability of MR sequences for the visualization of USPIO-labeled grafts. T1-, T2*-, and PD-weighted images of TEVG and iTEVG are shown on the left and right, respectively. As expected USPIO incorporation into the grafts leads to a decrease in signal intensity in all different MRI images, being most pronounced in T2*-weighted ones, which are highly sensitive for magnetic susceptibilities. However, in T2*-weighted images USPIO incorporation also leads to artefacts that may disturb further MRI characterization of the vessel lumen and the surrounding tissue. These artefacts are much less apparent in T1- and PD-weighted images; scale bar = 1 mm. C) Absolute quantification of the impact of USPIO incorporation into the meshes requires relaxometric analysis. R2 and R2* relaxation rates of iTEVG are higher than for TEVG, which underlines the relevance of this labelling. D) 3D rendering of a T2-weighted MRI dataset of a textile reinforcement in an iTEVG during bioreactor conditioning; scale bar = 1 mm. $P < 0.05$ was considered to represent statistical significance. (For interpretation of the references to colour in this figure legend, the reader is referred to the Web version of this article.)

USPIO labeling had no negative effect on tissue development *in vitro*. TEVG and iTEVG resisted a burst pressure of 872 ± 90 mmHg and 873 ± 266 mmHg, respectively, which is approximately 7-fold the systolic arterial blood pressure and therefore adequate for implantation in the systemic circulation. All grafts were easy to handle and suturable as illustrated in Fig. 4 O, showing a freshly implanted graft immediately after completion of distal and proximal anastomoses and before closure of the wound.

3.2. *In vivo longitudinal monitoring of the tissue-engineered grafts by MRI and PET-CT*

Five out of 6 animals had an uneventful operative procedure and survived until the predetermined study end point of 2 months with patent grafts. Complications during the implantation procedure occurred in one animal receiving a non-labeled TEVG. Specifically, during the initial phase of the implantation, one of the clamps, used to define the portion of vessel to be replaced with the TEVG, unexpectedly opened after the carotid artery segment had been excised. This resulted in the temporary loss of the implant in the operation wound and extensive manipulation to recover it. This probably caused significant endothelial damage resulting in a thrombotic event. The graft was found occluded by MRI four weeks after implantation. The animal also suffered from severe respiratory complications and was euthanized after the MRI examination. The quality of the MRI data for this animal was unfortunately not high enough to enable reliable quantification.

The other implanted tissue-engineered grafts were followed *in vivo* over an 8-week period according to the scheme shown in Fig. 1. Specifically: PET-CT was performed 1 and 3 weeks after implantation, while MRI was performed after 4 and 8 weeks. The choice of the time points for imaging was due to the limited availability of the clinically used MRI and PET-CT systems. PET is one of the most sensitive

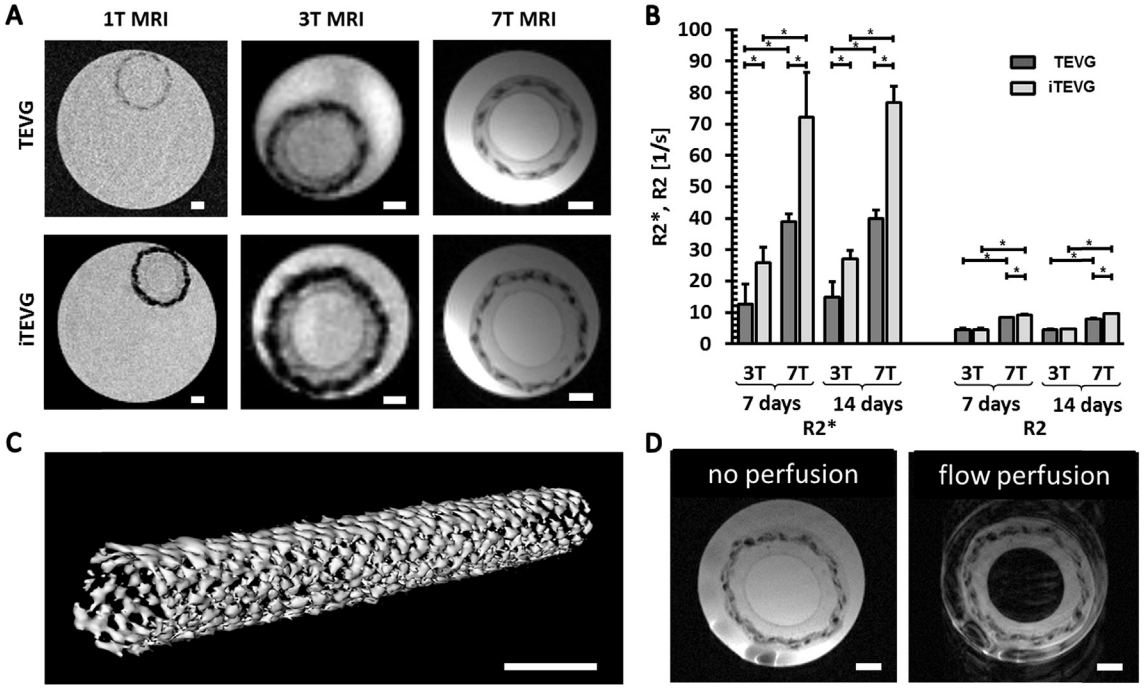

Fig. 3. MR characterization of TEVG and iTEVG prior to implantation at different magnetic field strengths. A) MR visualization using T2-weighted images for TEVG (top) and iTEVG (bottom) in 1T (left), 3T (middle) and 7T (right) MR scanners; scale bar = 1 mm. B) Quantitative analysis of R2 and R2* relaxation rates in 3T and 7T MR scanners for longitudinal evaluation of the grafts after 7 and 14 days in bioreactor conditioning. C) 3D rendering of a textile reinforcement in an iTEVG during bioreactor conditioning using a 7T MR scanner; scale bar = 5 mm. D) MR visualization using T2-weighted sequences for iTEVG under static (left) or flow (right) conditions; scale bar = 1 mm. $P < 0.05$ was considered to represent statistical significance. Data points represent the average R2* and R2 values for three different locations along the longitudinal axis of iTEVG (n = 1) and TEVG (n = 1) grafts.

molecular imaging techniques and has been used in the field of tissue engineering to monitor cellular functionality, adherence as well as metabolic activity in *in vitro* system [43,44]. In the vascular system, increased uptake of ^{18}F-FDG was reported as a sign of local inflammation [36,45,46]. With this technique, we detected a mild inflammation at the side of all the tissue-engineered grafts 1 week after implantation as indicated by the arrows in Fig. 5 A, B. The resolution of the PET images, however, did not allow for a precise attribution of the signal to specific anatomical locations, therefore an overlay with contrast-enhanced CT was performed (Fig. 5C). For all TE grafts, ^{18}F-FDG uptake was slightly higher than in the contralateral artery where a GORE-TEX® graft was implanted. However, the synthetic graft was implanted at an earlier time point (when the carotid was biopsied to obtain the autologous cells) and therefore probably not affected anymore by post-interventional inflammation. In one of the iTEVG, there was a noticeable increase in the average ^{18}F-FDG uptake at week 3, whereas in all other grafts, it stayed constant or decreased slightly, as expected from the inflammatory response after surgery. The same animal also presented a clearly higher ^{18}F-FDG uptake at the GORE-TEX® site with respect to week 1 and a slightly higher uptake at the carotid artery site (Fig. 5 D, indicated by black arrows). No significant difference between the ^{18}F-FDG uptake of TEVG and iTEVG was detected, nor between those of GORE-TEX® grafts and the carotid arteries of the two groups of animals at 4 and 8 weeks. It is known that iron-oxide nanoparticles can interfere with the biological activity of cells through the production of reactive oxygen species (ROS), depending on their size, concentration, surface charge, type of coating and functional groups [47–49]. However, in our case, only a very limited amount of USPIO could be in direct contact with cells, while the majority was embedded in the non-biodegradable textile fibers, thus not accessible to the cells over the time of the experiment.

MR imaging enabled longitudinal assessment of patency, position and function of the tissue-engineered vascular grafts. iTEVG could be visualized and precisely localized over time using PD-weighted MRI (Fig. 6). USPIO-labeling resulted in significantly enhanced contrast and maintained stability with only a small, non-significant decrease in the relaxation rate over the duration of this study (Fig. 6 B). This is a clear advantage of marking the textile scaffold as compared to the cellular component. Long-term observation of SPIO-labeled cells might be limited because of dilution of USPIO with cell divisions and decrease in labeled cell density due to their migration and integration into the host tissue [50] and extracellular deposition in tissues by active exocytosis [51] or cell death [52]. Guzman and colleagues found that the relative SPIO concentration was decreased by 50% every 3 days [50], however the same authors and others [53] were able to detect cell clusters for several weeks. An aspect to be considered is that deposited iron particles can be scavenged by macrophages, resulting in false MRI signals. Terrovitis and colleagues reported that 3 weeks after stem cell transplantation, few or no viable stem cells were present and that the significant iron-dependent MRI signal was attributed to ferumoxide-containing macrophages [52]. In this context it is noteworthy that Zhou et al. were able to monitor by T2-weighted MR scans tissue-engineered urethrae, which were fabricated by cellular sheets consisting of iron-labeled stem cells, for up to 3 months in beagle dogs. The authors, however, did not comment whether the iron was still located in the original cells [54].

No edema around the implants was observed. Five out of 6 tissue-engineered vascular grafts were confirmed to be freely perfused for up to 2 months post implantation by phase-contrast angiography (PCA), whereas all GORE-TEX® grafts were significantly or completely occluded by thrombus formation (Fig. 6 A) as also confirmed by visual inspection on the explanted grafts (Fig. 9 D). MRI of USPIO-labeled implants enabled their precise localization within the native artery as shown in Fig. 7 A and B. With respect to scans of the native artery in proximity of the anastomoses, a clear drop of the MRI signal was detected for the length of the iTEVG (Fig. 7 E). A meticulous investigation of the implant, as also demonstrated in Fig. S8, could be advantageous to properly localize and attribute events such collapse, aneurysm and

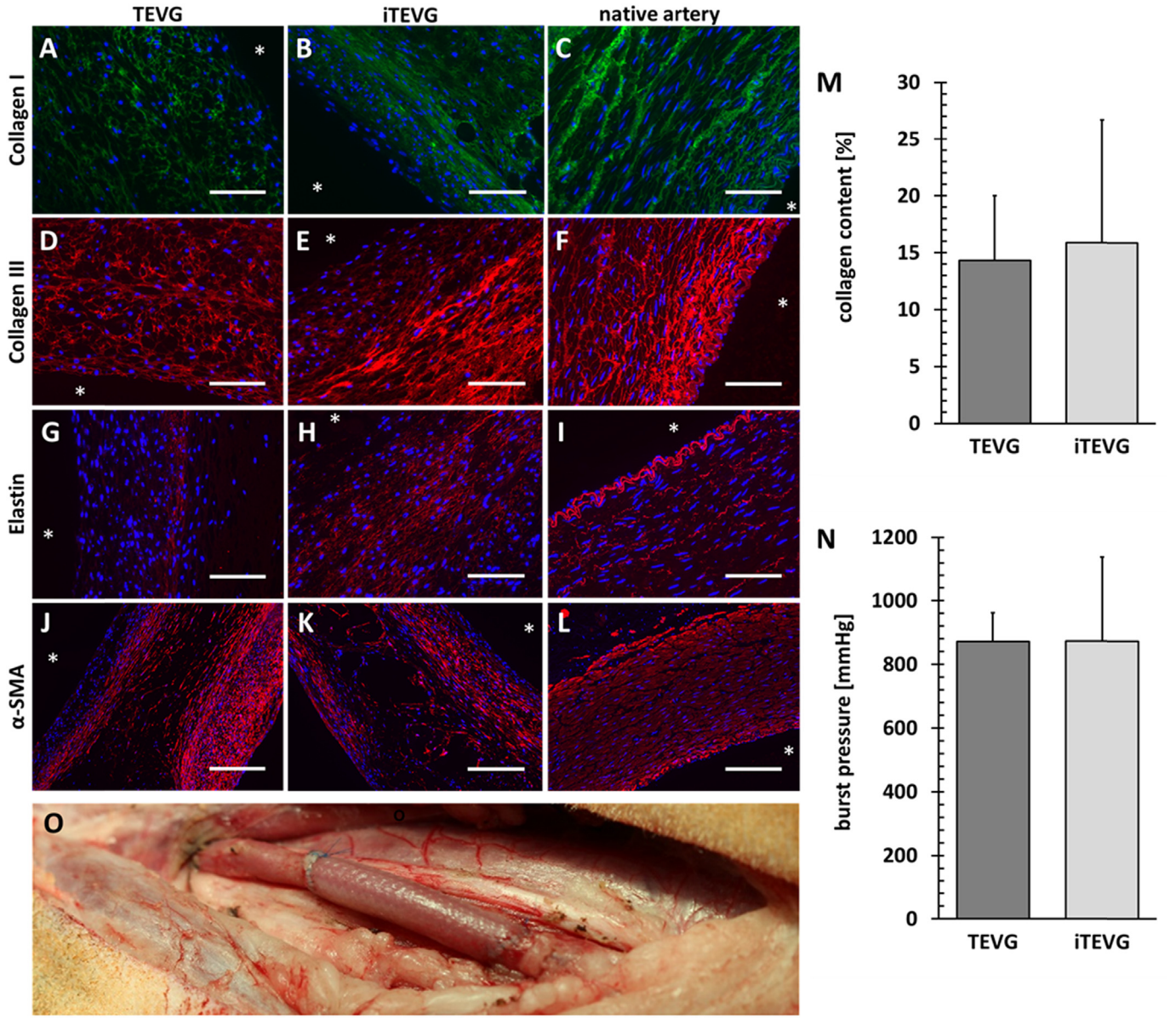

Fig. 4. Immunohistological, biochemical and mechanical analysis of tissue-engineered grafts prior to implantation. Staining against collagen type I (A–C) and collagen type III (D–F) revealed collagen synthesis during bioreactor conditioning. Elastin synthesis was detectable (G–I) and the majority of cells within the graft wall stained positive for α-SMA (J–L). A freshly explanted ovine carotid artery was used as positive control. Asterisks indicate the vessel lumen. Graphs illustrating the collagen content of TEVG (n = 3) and iTEVG (n = 3) in relation to ovine carotid artery (M) and the burst strength (N). Macroscopic appearance of the graft at implantation (O) before final closure of the wound. Scale bars: A-I = 100 µm, J-L = 200 µm.

thrombus formation to the graft or to the native vessel, which can facilitate decision-making with respect to pharmacological or surgical interventions. The exact delineation of the grafts' proximal and distal anastomoses was not possible by MRI of non-labeled grafts and by PET-CT for any of the grafts (Fig. 7C, D).

Ideally, the detailed information about the anatomical localization and function of the grafts provided by MRI is combined with PET to accurately monitor implant-associated inflammation. In comparison to CT, MRI offers the advantage of not requiring ionizing radiation and enabling angiography without contrast agents. At the time of study, a hybrid PET-MRI system was not available for animals of the size of sheep. Nevertheless, the importance of multimodal imaging could be exemplary shown in one of the animals for which PET-CT follow-up was logistically possible at additional time points. A drastic increase in the PET signal was detected at the side of implantation, six weeks after surgery (Fig. 8A–C). Here, the overlay of the PET data with the corresponding contrast enhanced CT data allowed the precise localization of the PET signal and revealed that, unexpectedly, an acute thrombotic event occurred in the jugular vein while the tissue-engineered vascular graft was not affected (Fig. 8E–G). Longitudinal monitoring in the following weeks indicated a clear decline of the PET signal and partial reopening of the vessel (Fig. 8 D, H). Inflammation can be detected within the first 3–4 weeks as a result of the operative intervention and the physiological remodeling of graft material and surrounding tissue. Furthermore, we cannot exclude trauma at the implantation site due to accidental collision. Infection, thrombosis and host versus graft reactions are further potential causes of inflammation. However, these would not be temporary and lead to loss of function of the graft without additional therapy. Therefore, the latter reasons are less probable to have caused inflammation in the case shown in Fig. 8, where the grafts were still functional after explantation and did not show peculiarities in histology. However, it would be of highest

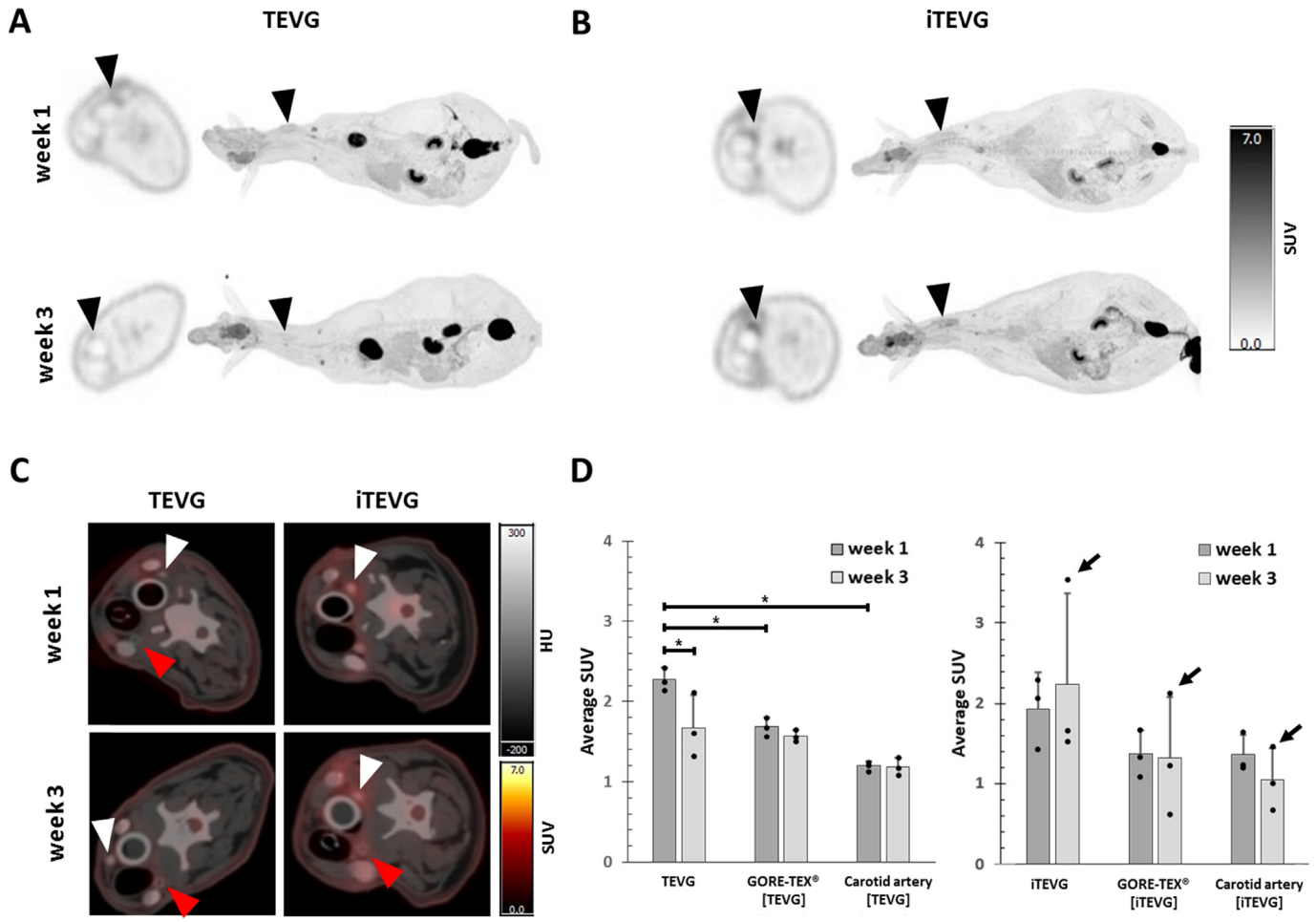

Fig. 5. PET-CT monitoring. Whole body PET of sheep models 1 and 3 weeks after A) TEVG (n = 3) and B) iTEVG (n = 3) implantation; black arrows indicate the site of implantation; C) Contrast enhanced PET- CT images of sheep necks 1 and 3 weeks after TEVG and iTEVG implantation into the left carotid artery; red arrows indicate occluded GORE-TEX® grafts; white arrows indicate TEVG and iTEVG; D) Quantification of ^{18}F-FDG uptake at the implantation site of TEVG, iTEVG and GORE-TEX® grafts and at the caudal part of the left carotid artery; black arrows indicate the values relative to one animal. $P < 0.05$ was considered to represent statistical significance. (For interpretation of the references to colour in this figure legend, the reader is referred to the Web version of this article.)

importance to detect and treat such serious complications. Thus, imaging is recommended at 3–4 weeks, when the postoperative inflammation should have decreased to baseline. In case of persistent or increasing inflammation follow up monitoring should be performed and will help to assess the efficacy of therapeutic interventions.

The importance of multimodal imaging for the evaluation of tissue-engineered implants has been also shown by Stacy et al. who demonstrated the non-invasive assessment of matrix metalloproteinase activity to evaluate the remodeling process of TEVG implanted in a growing large animal model by hybrid single photon emission CT (SPECT)/CT imaging [55].

3.3. Tissue analysis of explanted tissue-engineered grafts

Post-explantation tissue analyses included macroscopic assessment of the explant lumen and the histological, immunohistochemical, biochemical, as well as mechanical evaluation of the tissue properties. Macroscopic evaluation of the explants' luminal surfaces showed no signs of thrombus or aneurysm formation and smooth transitions at the anastomoses (Fig. 9A–B). No differences could be observed between USPIO-labeled and non-labeled implants.

Immunohistochemical staining proved the formation of an endothelial cell monolayer lining at the luminal side of all explanted tissue-engineered vascular grafts (Fig. 9E–H). Van Kossa staining demonstrated large calcified areas in all GORE-TEX® control grafts, which were implanted as carotid artery interposition grafts at the contralateral side when biopsies for cell isolation were harvested. All tissue-engineered vascular grafts were free of any calcific deposits (Fig. 9I–L).

Explanted tissue-engineered vascular grafts stained positive for collagen type I and III (Fig. 9M–R). Furthermore, *in vivo* tissue maturation led to a significant increase in elastin deposition throughout the vessel wall (Fig. 9S–U). Elastin synthesis *in vivo* has been shown for decellularized vascular grafts as a marker for remodeling [56], clearly supporting the potential of these grafts. However, to the best of our knowledge, a native-like internal elastic lamina has not been reported and the contribution of the synthesized elastin to the tensile mechanical properties of the grafts still needs to be demonstrated.

The vast majority of cells in the vessel wall stained positive for α-SMA and were oriented in the circumferential direction as in the native artery (Fig. 9V–X).

Using the hydroxyproline assay an increased collagen content was found in both the TEVG and the iTEVG resulting from extensive *in vivo* tissue remodeling, reaching even higher values than those of the native carotid artery (Fig. 9 Y). This is often observed in tissue-engineered vascular substitutes in the course of their *in vivo* integration, independent of the fabrication strategy used to produce them [56–61]. Studies have shown that the collagen content can increase, remain constant or even decrease over time depending on the matrix metalloproteinase activity defining the stage of the remodeling/healing process [22,55,57,60]. However, the collagen content in the iTEVG was

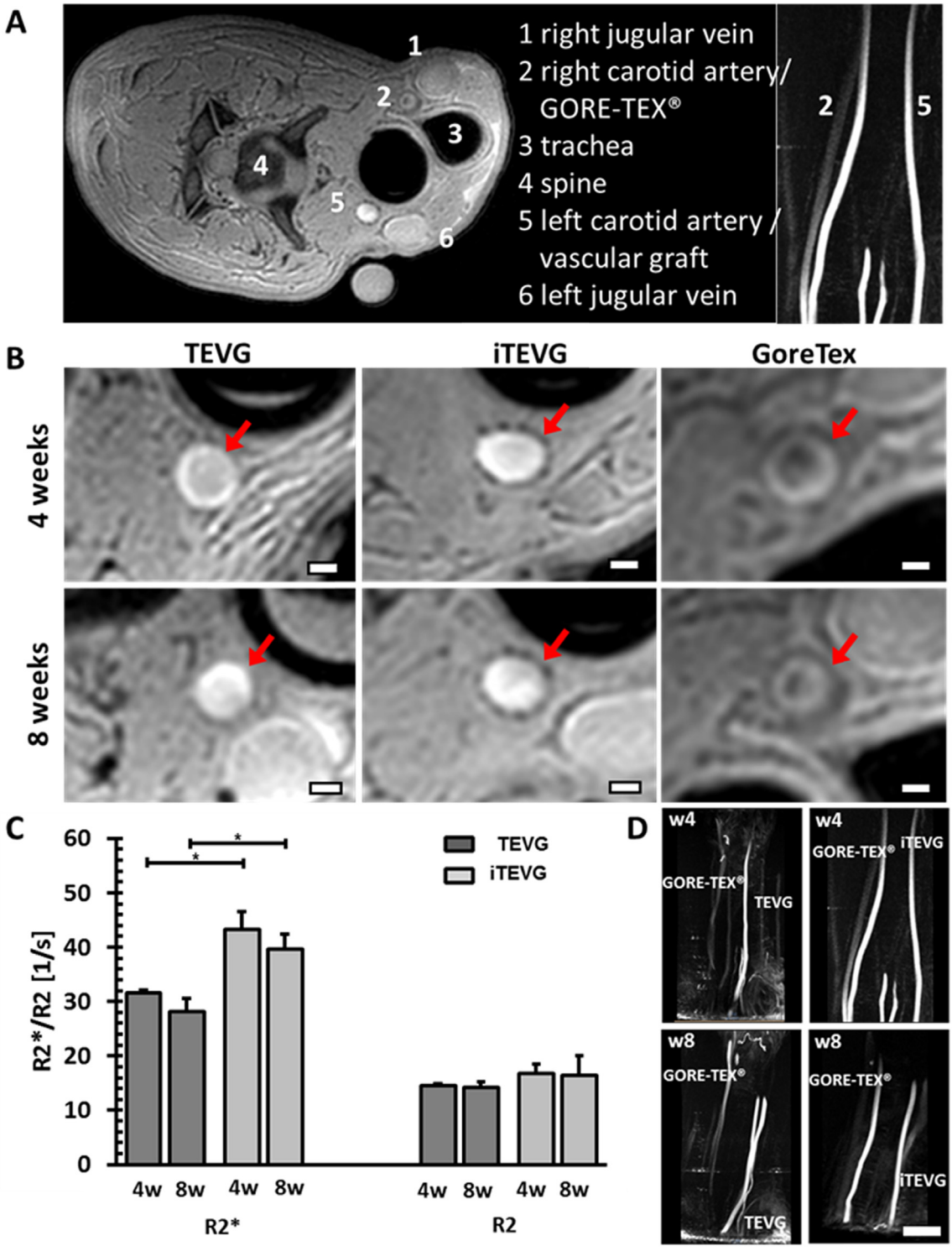

Fig. 6. In vivo MRI longitudinal monitoring. A) MRI scan of the region of interest with anatomical details and corresponding MRI angiography; B) MR images of TEVG, iTEVG and GORE-TEX® grafts 4 and 8 weeks post-implantation; scale bar = 5 mm. C) Quantification of R2* and R2 relaxation rates of TEVG and iTEVG after 4 (n(iTEVG) = 3, n(TEVG) = 2) and 8 weeks (n(iTEVG) = 3, n(TEVG) = 2); D) MR angiography of the grafts presented in B. The complete lack of MRI signal in the GORE-TEX® graft is due to the thrombotic occlusion of the graft; scale bar = 5 cm. $P < 0.05$ was considered to represent statistical significance.

not significantly higher than in TEVG, indicating, that the introduction of the USPIO particles into the textile did not significantly influence the tissue remodeling, while enabling the monitoring of the graft, supporting the quality control in the *in vitro* phase and the functional assessment *in vivo*.

Successful MRI visualization of iron oxide nanoparticle-loaded hernia meshes has been reported in preclinical and clinical trials, where the postoperative mesh deformation and associated loss of total mesh surface could be reliably determined [62–65]. As in the present study, PVDF fibers were used to produce the textile meshes. It is our strategy to use a non-degradable mesh to avoid long-term loss of functionality as dilation, aneurysm formation and structural deterioration are main failure mechanisms of tissue-engineered vascular grafts [4,66]. However, the USPIO labeling is not limited to non-biodegradable materials

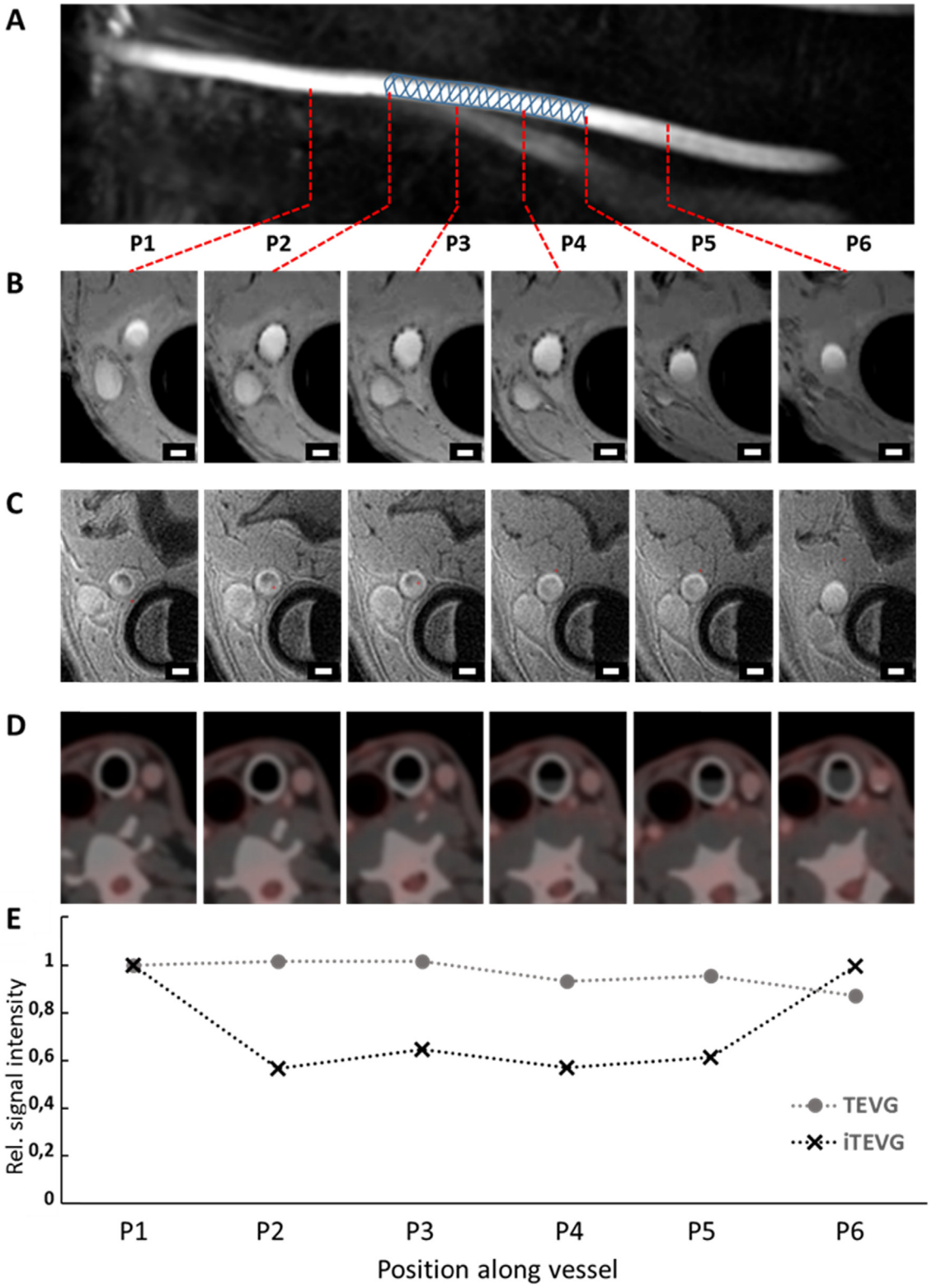

Fig. 7. Precise localization of an iTEVG *in vivo* by MRI. A) Schematic representation of the implantation site. B) The presence of the USPIO allowed to distinguish between the tissue-engineered vascular graft and the native vessel (two outer scans in the sequence); scale bar = 5 mm. This same precision could not be achieved for C) TEVG or D) by PET-CT; scale bar = 5 mm. E) MRI relative signal intensity for the scans shown in B and C, with respect to the signal in the outer scans of the sequences.

and ongoing work in our groups aims at developing imageable bioresorbable textiles. The concept followed in this study relies on the passive embedding of the USPIO particles during polymer fiber extrusion. However, other tissue-engineering approaches for vascular grafts could also benefit from USPIO-enabled MRI monitoring as, for example, decellularized vessels [67]. The USPIO-labelling of such collagen-rich matrixes can be achieved by covalent conjugation of carboxyl-functionalized USPIO particles to collagen via carboxyl-to-amine crosslinking

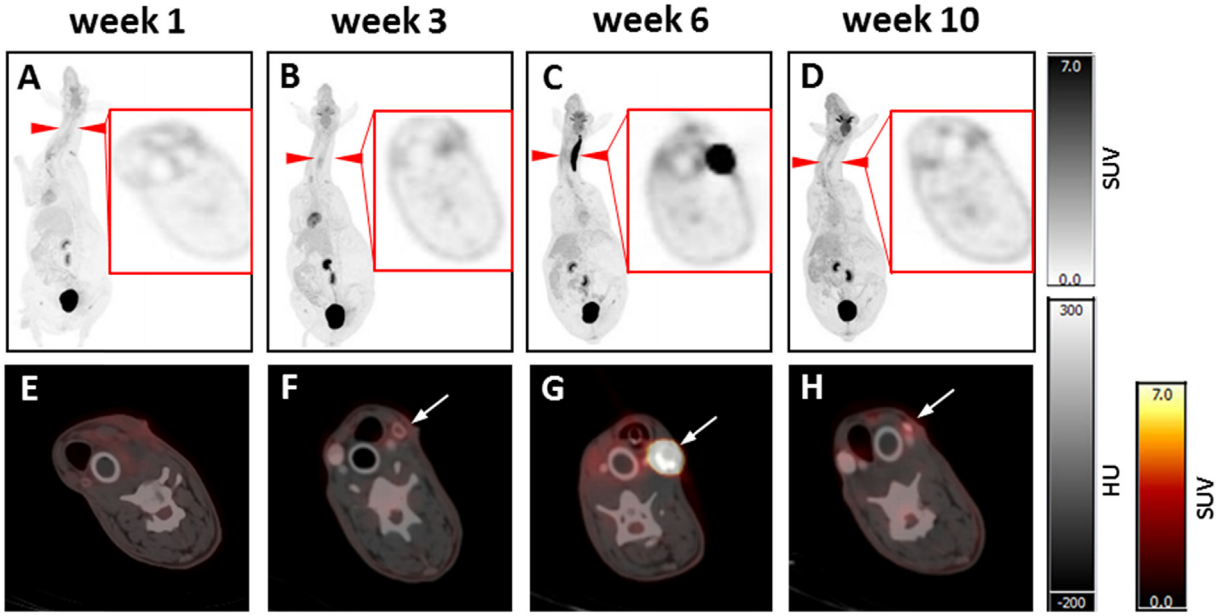

Fig. 8. Longitudinal monitoring by PET-CT. A-D) PET images showed a drastic increase in the uptake of ^{18}F-FDG at week 6. E) CT provided higher resolution images with respect to PET, however exact localization of the PET signal was only possible through contrast-enhanced CT-PET overlays (F–H). The presence of the TEVG could be excluded as cause of the inflammation. The white arrows indicate the jugular vein where a thrombus is evident at week 3, followed by an acute inflammation (week 6) which faded away by week 10 with partial opening of the vessel.

or alternatively by covalent conjugation of amine-functionalized USPIOs using EDC/NHS chemistry (1-ethyl-3-(3-dimethylaminopropyl) carbodiimide (EDC); n-hydroxysuccinimide (NHS)) as shown by Mertens et al. for collagen-based scaffolds [27]. With such a procedure, however, the particles will be in direct contact with the cells.

Non-invasive monitoring of *in vivo* hydrogel degradation by MRI was successfully achieved with USPIO-labeled cellulose nanocrystal/silk fibroin hydrogels during cartilage regeneration in a rabbit cartilage defect model for 3 months [68]. A gadolinium-based complex was covalently linked to an injectable hyaluronic acid hydrogel to enable T1- and T2-weighted MRI [69]. Bakker and colleagues recently developed a gadolinium-based MRI contrast agent designed to supramolecularly interact with an ureidopyrimidinone-based hydrogel to enable high-quality imaging, as demonstrated after targeted intramyocardial hydrogel injection in a pig heart [70]. Recently, a naturally derived hemin-L-lysine (HL) complex was used to label hybrid templates composed of collagen type I reinforced with degradable polymers that were subcutaneously implanted in mice. This enabled the longitudinal visualization by MRI with good contrast and in correlation with scaffold remodeling [71]. Alternatively to ^{1}H MRI as performed in this study, ^{19}F MRI can also be applied to image vascular scaffolds if novel fluorinated polymeric materials are incorporated that possess magnetically visible ^{19}F atoms with high mobility, enabled by the amorphous structure of the polymers [72].

CT has also been employed to follow the fate of implanted acellular scaffolds as in the case of electrospun vascular grafts in rats [21], and alginate and agarose hydrogels in mice [73]. In both studies, the scaffold material had to be doped to be distinguishable from the surrounding soft tissue. Forton et al. used highly radiopaque gadolinium oxide nanocrystals and were able to follow the implants over 23 weeks by serial microCT with a resolution higher than the one achievable by MRI. The implant elicited a typical mild foreign body reaction, no leaching out or dissolution of the gadolinium oxide was detected, however blood work revealed reduced hematopoiesis. While extrapolation to humans and clinically used X-ray systems is not straightforward, the reported X-ray induced effect is rather worrisome and also the long term tissue deposition of the highly toxic gadolinium requires further investigation [73]. Furthermore, in comparison to MRI, the tissue contrast of CT is worse and thus, it will be difficult to use this imaging modality to monitor the remodeling of the scaffolds *in vivo*, which often is an important indicator of their long term functionality. Further imaging modalities to follow the fate of implanted tissue-engineered scaffolds are ultrasound and photoacoustic imaging [74]. While ultrasound can favorably be used to monitor the functionality of a tissue-engineered vascular graft as well as its anatomical integrity (e.g. wall thickness or aneurysm formation), photoacoustic imaging can also provide insights into blood oxygenation in the implant as well as its microvascularization. However, both modalities suffer from user dependence and limited reproducibility, which need to be considered, particularly when performing longitudinal observations in larger animals and humans.

Overall, the modification of materials to render them compatible with clinically applied techniques represent a realistic strategy to advance the adoption of the grafts in the clinic in a fast way with the approval of the clinicians. We here showed that labeling textiles with USPIO enables the longitudinal monitoring of tissue-engineered vascular grafts *in vitro* and *in vivo*.

4. Conclusions

We here show the fabrication and *in vivo* evaluation of imageable textile-reinforced biohybrid vascular grafts. The grafts underwent remarkable remodeling within 8 weeks and showed excellent functionality. Our results demonstrate the non-invasive longitudinal monitoring of these constructs with techniques widely applied in the clinic. We were able to combine MR data on the localization and function of the graft with molecular PET data on macrophages-mediated inflammation. The capability of obtaining more accurate and complete information by multimodal imaging is a critical aspect towards the translation of tissue-engineered vascular grafts to the clinical settings.

Data availability

The data associated with this manuscript is available upon request to the corresponding authors.

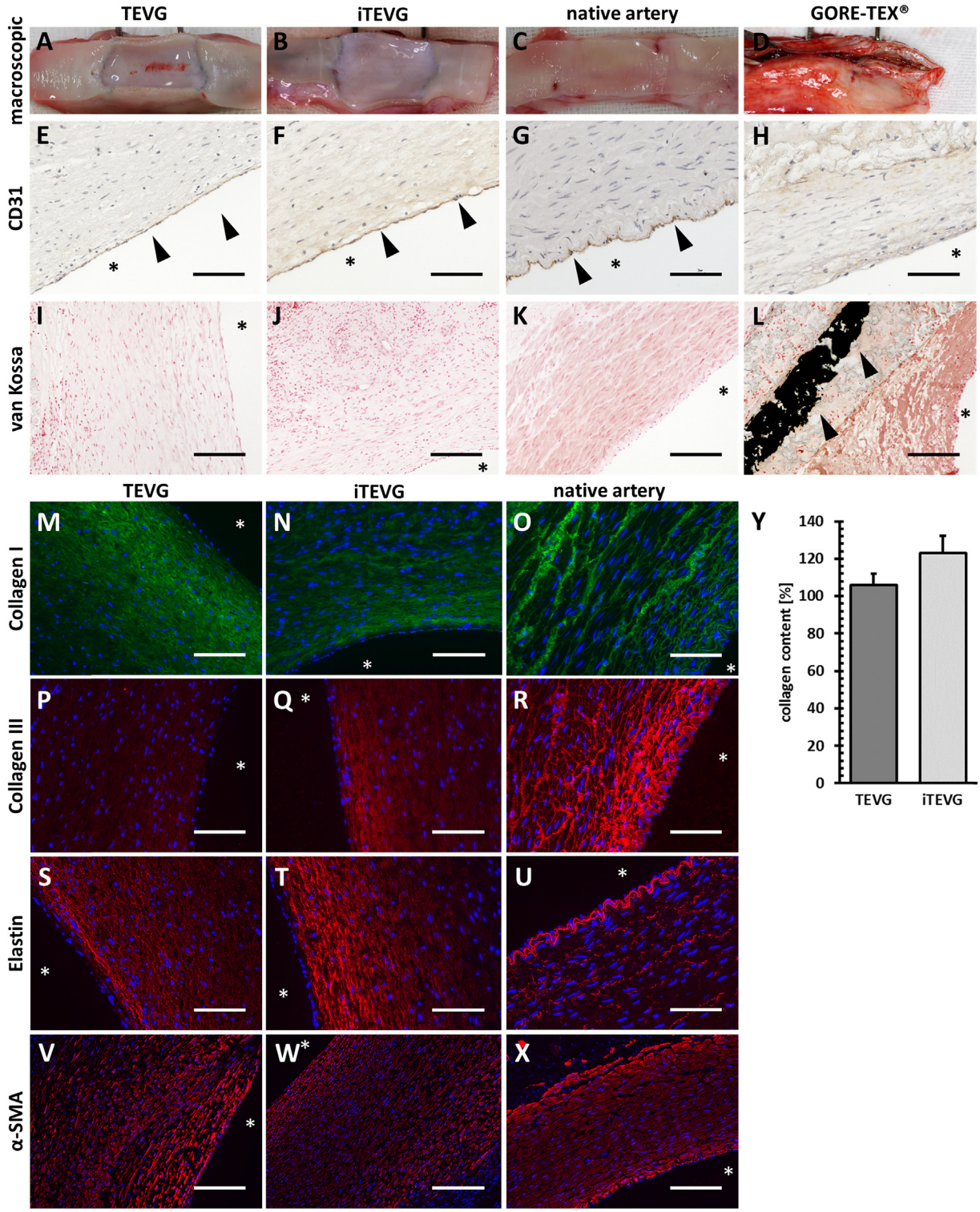

Fig. 9. Macroscopic view of the luminal surface of the explanted grafts and tissue analysis. A-D) No thrombus formation was evident in TEVG and iTEVG, whereas the GORE-TEX® controls showed significant thrombus formation and occlusion. E-H) Endothelial coverage of the luminal surface was observed in tissue-engineered vascular grafts by CD 31 staining. Arrow heads indicate the endothelial layer; I-L) Calcifications were not detected in tissue-engineered vascular grafts by van Kossa staining, whereas GORE-TEX® control grafts showed massive calcific depositions (arrow heads). M − O) Staining against collagen type I, P-R) collagen type III and S–U) elastin revealed extensive tissue remodeling *in vivo*; V-X) The vast majority of cells in the vessel wall stained positive for α-SMA. A freshly explanted ovine carotid artery was used as positive control. Asterisks indicate the vessel lumen. Scale bars: E-H = 50 μm, I–U = 100 μm, V-X = 200 μm; Y) Collagen content as percentage of that of the native carotid artery for TEVG (n = 2) and iTEVG (n = 3).

Acknowledgements

This work was funded by NRW/EU-Ziel 2-Programm (EFRE) 2007–2013: “Entwicklung und Bildgebung patientenoptimierter Implantate”, the European Research Council (ERC Starting Grant 309495: NeoNaNo, the Integrated Interdisciplinary Institute of Technology for Medicine (I3TM) of RWTH Aachen University through the Seed-Funds SF-2018_02_05 and SF 16-6-01, and the German Research Foundation (DFG – Project number: 403039938).

Appendix A. Supplementary data

Supplementary data to this article can be found online at https://doi.org/10.1016/j.biomaterials.2019.119228.

Author contributions

FW and SK prepared the tissue-engineered vascular grafts and were responsible of the study's coordination. FW, SK, AR and PM performed the tissue analysis and interpretation. SJ, TL, FM and FK were responsible for the study design. VF, MM and NG-W performed the in vitro and in vivo MR monitoring of grafts and the MRI data analysis together with TL, FK, PM and FW. OW and AM performed the PET- CT monitoring of grafts and the data analysis together with FM, PM and FW. HS and KC were responsible for the surgical implantation of the grafts. FW, PM, TL, FK wrote the manuscript. All authors discussed the results and approved the final version of the manuscript.

References

[1] R. Langer, J.P. Vacanti, Tissue engineering, Science 260 (5110) (1993) 920–926.
[2] L.F. Tapias, H.C. Ott, Decellularized scaffolds as a platform for bioengineered organs, Curr. Opin. Organ Transplant. 19 (2) (2014) 145–152.
[3] M. Wilhelmi, S. Jockenhoevel, P. Mela, Bioartificial fabrication of regenerating blood vessel substitutes: requirements and current strategies, Biomed. Tech. 59 (3) (2014) 185–195.
[4] T.B. Wissing, V. Bonito, C.V.C. Bouten, A.I.P.M. Smits, Biomaterial-driven in situ cardiovascular tissue engineering - a multi-disciplinary perspective, npj Regenerative Medicine 2 (18) (2017).
[5] A. Khademhosseini, R. Langer, A decade of progress in tissue engineering, Nat. Protoc. 11 (10) (2016) 1775–1781.
[6] J.H. Lawson, M.H. Glickman, M. Ilzecki, T. Jakimowicz, A. Jaroszynski, E.K. Peden, A.J. Pilgrim, H.L. Prichard, M. Guziewicz, S. Przywara, J. Szmidt, J. Turek, W. Witkiewicz, N. Zapotoczny, T. Zubilewicz, L.E. Niklason, Bioengineered human acellular vessels for dialysis access in patients with end-stage renal disease: two phase 2 single-arm trials, Lancet 387 (10032) (2016) 2026–2034.
[7] M. Olausson, P.B. Patil, V.K. Kuna, P. Chougule, N. Hernandez, K. Methe, C. Kullberg-Lindh, H. Borg, H. Ejnell, S. Sumitran-Holgersson, Transplantation of an allogeneic vein bioengineered with autologous stem cells: a proof-of-concept study, Lancet 380 (9838) (2012) 230–237.
[8] N. Hibino, E. McGillicuddy, G. Matsumura, Y. Ichihara, Y. Naito, C. Breuer, T. Shinoka, Late-term results of tissue-engineered vascular grafts in humans, J. Thorac. Cardiovasc. Surg. 139 (2) (2010) 431-6, 436 e1-2.
[9] L.A. Bockeria, O. Svanidze, A. Kim, K. Shatalov, V. Makarenko, M. Cox, T. Carrel, Total cavopulmonary connection with a new bioabsorbable vascular graft: first clinical experience, J. Thorac. Cardiovasc. Surg. 153 (6) (2017) 1542–1550.
[10] F. Colombo, G. Sampogna, G. Cocozza, S.Y. Guraya, A. Forgione, Regenerative medicine: clinical applications and future perspectives, J Microsc Ultrastruct 5 (1) (2017) 1–8.
[11] V.J. Mase Jr., J.R. Hsu, S.E. Wolf, J.C. Wenke, D.G. Baer, J. Owens, S.F. Badylak, T.J. Walters, Clinical application of an acellular biologic scaffold for surgical repair of a large, traumatic quadriceps femoris muscle defect, Orthopedics 33 (7) (2010) 511.
[12] Z. Xiao, F. Tang, J. Tang, H. Yang, Y. Zhao, B. Chen, S. Han, N. Wang, X. Li, S. Cheng, G. Han, C. Zhao, X. Yang, Y. Chen, Q. Shi, S. Hou, S. Zhang, J. Dai, One-year clinical study of NeuroRegen scaffold implantation following scar resection in complete chronic spinal cord injury patients, Sci. China Life Sci. 59 (7) (2016) 647–655.
[13] J. Frese, A. Morgenroth, M.E. Mertens, S. Koch, L. Rongen, A.T. Vogg, B.D. Zlatopolskiy, B. Neumaier, V.N. Gesche, T. Lammers, T. Schmitz-Rode, P. Mela, S. Jockenhoevel, F.M. Mottaghy, F. Kiessling, Nondestructive monitoring of tissue-engineered constructs, Biomed. Tech. 59 (2) (2014) 165–175.
[14] L. Teodori, A. Crupi, A. Costa, A. Diaspro, S. Melzer, A. Tarnok, Three-dimensional imaging technologies: a priority for the advancement of tissue engineering and a challenge for the imaging community, J. Biophot. 10 (1) (2017) 24–45.
[15] K. Kim, W.R. Wagner, Non-invasive and non-destructive characterization of tissue engineered constructs using ultrasound imaging technologies: a review, Ann. Biomed. Eng. 44 (3) (2016) 621–635.
[16] A.J. Neumann, T. Quinn, S.J. Bryant, Nondestructive evaluation of a new hydrolytically degradable and photo-clickable PEG hydrogel for cartilage tissue engineering, Acta Biomater. 39 (2016) 1–11.
[17] M.A. Rice, K.R. Waters, K.S. Anseth, Ultrasound monitoring of cartilaginous matrix evolution in degradable PEG hydrogels, Acta Biomater. 5 (1) (2009) 152–161.
[18] S. Kreitz, G. Dohmen, S. Hasken, T. Schmitz-Rode, P. Mela, S. Jockenhoevel, Nondestructive method to evaluate the collagen content of fibrin-based tissue engineered structures via ultrasound, Tissue Eng. C Methods 17 (10) (2011) 1021–1026.
[19] L.G. Hurtado-Aguilar, S. Mulderrig, R. Moreira, N. Hatam, J. Spillner, T. Schmitz-Rode, S. Jockenhoevel, P. Mela, Ultrasound for in vitro, noninvasive real-time monitoring and evaluation of tissue-engineered heart valves, Tissue Eng. C Methods 22 (10) (2016) 974–981.
[20] P. Maschhoff, S. Heene, A. Lavrentieva, T. Hentrop, C. Leibold, M.-N. Wahalla, N. Stanislawski, H. Blume, T. Scheper, C. Blume, An intelligent bioreactor system for the cultivation of a bioartificial vascular graft, Engineering in life scieces 17 (5) (2017) 567–578.
[21] H. Talacua, S.H.M. Söntjens, S.H. Thakkar, A.M.A. Brizard, L.A. van Herwerden, A. Vink, G.C. van Almen, P.Y.W. Dankers, C.V.C. Bouten, R.P.J. Budde, H.M. Janssen, J. Kluin, Monitoring in vivo degradation of an electrospun vascular graft for in situ tissue engineering by CT-imaging, Situ Cardiovascular Tissue Engineering, 2016.
[22] M.R. Stacy, C.A. Best, M.W. Maxfield, M. Qiu, Y. Naito, H. Kurobe, N. Mahler, K.A. Rocco, A.J. Sinusas, T. Shinoka, S. Sampath, C.K. Breuer, Magnetic resonance imaging of shear stress and wall thickness in tissue-engineered vascular grafts, Tissue Eng. C Methods 24 (8) (2018) 465–473.
[23] A. Berdichevski, H. Simaan Yameen, H. Dafni, M. Neeman, D. Seliktar, Using bimodal MRI/fluorescence imaging to identify host angiogenic response to implants, Proc. Natl. Acad. Sci. U. S. A. 112 (16) (2015) 5147–5152.
[24] J. Liu, K. Wang, J. Luan, Z. Wen, L. Wang, Z. Liu, G. Wu, R. Zhuo, Visualization of in situ hydrogels by MRI in vivo, J. Mater. Chem. B (4) (2016) 1343–1353.
[25] E. Bible, F. Dell'Acqua, B. Solanky, A. Balducci, P.M. Crapo, S.F. Badylak, E.T. Ahrens, M. Modo, Non-invasive imaging of transplanted human neural stem cells and ECM scaffold remodeling in the stroke-damaged rat brain by (19)F- and diffusion-MRI, Biomaterials 33 (10) (2012) 2858–2871.
[26] J.I. Kim, B.S. Lee, C. Chun, J.K. Cho, S.Y. Kim, S.C. Song, Long-term theranostic hydrogel system for solid tumors, Biomaterials 33 (7) (2012) 2251–2259.
[27] M.E. Mertens, A. Hermann, A. Buhren, L. Olde-Damink, D. Mockel, F. Gremse, J. Ehling, F. Kiessling, T. Lammers, Iron oxide-labeled collagen scaffolds for non-invasive MR imaging in tissue engineering, Adv. Funct. Mater. 24 (6) (2014) 754–762.
[28] M. Gauberti, A. Montagne, A. Quenault, D. Vivien, Molecular magnetic resonance imaging of brain-immune interactions, Front. Cell. Neurosci. 8 (2014) 389.
[29] E. Bull, S.Y. Madani, R. Sheth, A. Seifalian, M. Green, A.M. Seifalian, Stem cell tracking using iron oxide nanoparticles, Int. J. Nanomed. 9 (2014) 1641–1653.
[30] R.A. Revia, M. Zhang, Magnetite nanoparticles for cancer diagnosis, treatment, and treatment monitoring: recent advances, Mater. Today 19 (3) (2016) 157–168.
[31] D.H. Kim, J. Chen, R.A. Omary, A.C. Larson, MRI visible drug eluting magnetic microspheres for transcatheter intra-arterial delivery to liver tumors, Theranostics 5 (5) (2015) 477–488.
[32] G.N. Nelson, J.D. Roh, T.L. Mirensky, Y. Wang, T. Yi, G. Tellides, J.S. Pober, P. Shkarin, E.M. Shapiro, W.M. Saltzman, X. Papademetris, T.M. Fahmy, C.K. Breuer, Initial evaluation of the use of USPIO cell labeling and noninvasive MR monitoring of human tissue-engineered vascular grafts in vivo, FASEB J. 22 (11) (2008) 3888–3895.
[33] H. Perea, J. Aigner, J.T. Heverhagen, U. Hopfner, E. Wintermantel, Vascular tissue engineering with magnetic nanoparticles: seeing deeper, J. Tissue Eng. Regenerat. Med. 1 (4) (2007) 318–321.
[34] M.E. Mertens, J. Frese, D.A. Bolukbas, L. Hrdlicka, S. Golombek, S. Koch, P. Mela, S. Jockenhovel, F. Kiessling, T. Lammers, FMN-coated fluorescent USPIO for cell labeling and non-invasive MR imaging in tissue engineering, Theranostics 4 (10) (2014) 1002–1013.
[35] M.E. Mertens, S. Koch, P. Schuster, J. Wehner, Z. Wu, F. Gremse, V. Schulz, L. Rongen, F. Wolf, J. Frese, V.N. Gesche, M. van Zandvoort, P. Mela, S. Jockenhoevel, F. Kiessling, T. Lammers, USPIO-labeled textile materials for non-invasive MR imaging of tissue-engineered vascular grafts, Biomaterials 39 (2015) 155–163.
[36] J. Bucerius, Monitoring vasculitis with 18F-FDG PET, Q. J. Nucl. Med. Mol. Imaging 60 (3) (2016) 219–235.
[37] S. Koch, T.C. Flanagan, J.S. Sachweh, F. Tanios, H. Schnoering, T. Deichmann, V. Ella, M. Kellomaki, N. Gronloh, T. Gries, R. Tolba, T. Schmitz-Rode, S. Jockenhoevel, Fibrin-polylactide-based tissue-engineered vascular graft in the arterial circulation, Biomaterials 31 (17) (2010) 4731–4739.
[38] J. Jayapaul, M. Hodenius, S. Arns, W. Lederle, T. Lammers, P. Comba, F. Kiessling, J. Gaetjens, FMN-coated fluorescent iron oxide nanoparticles for RCP-mediated targeting and labeling of metabolically active cancer and endothelial cells, Biomaterials 32 (25) (2011) 5863–5871.
[39] G.K. Reddy, C.S. Enwemeka, A simplified method for the analysis of hydroxyproline in biological tissues, Clin. Biochem. 29 (3) (1996) 225–229.
[40] F. Gremse, M. Stark, J. Ehling, J.R. Menzel, T. Lammers, F. Kiessling, Imalytics preclinical: interactive analysis of biomedical volume data, Theranostics 6 (3) (2016) 328–341.
[41] P.J.A. Oomen, M.A.J. van Kelle, C.W.J. Oomens, C.V.C. Bouten, S. Loerakker, Nondestructive mechanical characterization of developing biological tissues using

inflation testing, J. Mech. Behav. Biomed. Mater. 74 (2017) 438–447.
[42] F. Wolf, D.M. Rojas Gonzalez, U. Steinseifer, M. Obdenbusch, W. Herfs, C. Brecher, S. Jockenhoevel, P. Mela, T. Schmitz-Rode, VascuTrainer: a mobile and disposable bioreactor system for the conditioning of tissue-engineered vascular grafts, Ann. Biomed. Eng. 46 (4) (2018) 616–626.
[43] T. Kofidis, A. Lenz, J. Boublik, P. Akhyari, B. Wachsmann, K. Mueller-Stahl, M. Hofmann, A. Haverich, Pulsatile perfusion and cardiomyocyte viability in a solid three-dimensional matrix, Biomaterials 24 (27) (2003) 5009–5014.
[44] H. Mertsching, T. Walles, M. Hofmann, J. Schanz, W.H. Knapp, Engineering of a vascularized scaffold for artificial tissue and organ generation, Biomaterials 26 (33) (2005) 6610–6617.
[45] A. Tawakol, R.Q. Migrino, U. Hoffmann, S. Abbara, S. Houser, H. Gewirtz, J.E. Muller, T.J. Brady, A.J. Fischman, Noninvasive in vivo measurement of vascular inflammation with F-18 fluorodeoxyglucose positron emission tomography, J. Nucl. Cardiol. 12 (3) (2005) 294–301.
[46] J. Bucerius, V. Mani, C. Moncrieff, J. Machac, V. Fuster, M.E. Farkouh, A. Tawakol, J.H. Rudd, Z.A. Fayad, Optimizing 18F-FDG PET/CT imaging of vessel wall inflammation: the impact of 18F-FDG circulation time, injected dose, uptake parameters, and fasting blood glucose levels, Eur. J. Nucl. Med. Mol. Imaging 41 (2) (2014) 369–383.
[47] H. Wu, J.J. Yin, W.G. Wamer, M. Zeng, Y.M. Lo, Reactive oxygen species-related activities of nano-iron metal and nano-iron oxides, J. Food Drug Anal. 22 (1) (2014) 86–94.
[48] A. Abdal Dayem, M.K. Hossain, S.B. Lee, K. Kim, S.K. Saha, G.M. Yang, H.Y. Choi, S.G. Cho, The role of reactive oxygen species (ROS) in the biological activities of metallic nanoparticles, Int. J. Mol. Sci. 18 (1) (2017).
[49] Z. Yarjanli, K. Ghaedi, A. Esmaeili, S. Rahgozar, A. Zarrabi, Iron oxide nanoparticles may damage to the neural tissue through iron accumulation, oxidative stress, and protein aggregation, BMC Neurosci. 18 (1) (2017) 51.
[50] R. Guzman, N. Uchida, T.M. Bliss, D. He, K.K. Christopherson, D. Stellwagen, A. Capela, J. Greve, R.C. Malenka, M.E. Moseley, T.D. Palmer, G.K. Steinberg, Long-term monitoring of transplanted human neural stem cells in developmental and pathological contexts with MRI, Proc. Natl. Acad. Sci. U. S. A. 104 (24) (2007) 10211–10216.
[51] S.M. Cromer Berman, Kshitiz, C.J. Wang, I. Orukari, A. Levchenko, J.W. Bulte, P. Walczak, Cell motility of neural stem cells is reduced after SPIO-labeling, which is mitigated after exocytosis, Magn. Reson. Med. 69 (1) (2013) 255–262.
[52] J. Terrovitis, M. Stuber, A. Youssef, S. Preece, M. Leppo, E. Kizana, M. Schar, G. Gerstenblith, R.G. Weiss, E. Marban, M.R. Abraham, Magnetic resonance imaging overestimates ferumoxide-labeled stem cell survival after transplantation in the heart, Circulation 117 (12) (2008) 1555–1562.
[53] C. Heyn, C.V. Bowen, B.K. Rutt, P.J. Foster, Detection threshold of single SPIO-labeled cells with FIESTA, Magn. Reson. Med. 53 (2) (2005) 312–320.
[54] S. Zhou, R. Yang, Q. Zou, K. Zhang, T. Yin, W. Zhao, J.G. Shapter, G. Gao, Q. Fu, Fabrication of tissue-engineered bionic urethra using cell sheet technology and labeling by ultrasmall superparamagnetic iron oxide for full-thickness urethral reconstruction, Theranostics 7 (9) (2017) 2509–2523.
[55] M.R. Stacy, Y. Naito, M.W. Maxfield, H. Kurobe, S. Tara, C. Chan, K.A. Rocco, T. Shinoka, A.J. Sinusas, C.K. Breuer, Targeted imaging of matrix metalloproteinase activity in the evaluation of remodeling tissue-engineered vascular grafts implanted in a growing lamb model, J. Thorac. Cardiovasc. Surg. 148 (5) (2014) 2227–2233.
[56] Z. Syedain, J. Reimer, M. Lahti, J. Berry, S. Johnson, R.T. Tranquillo, Tissue engineering of acellular vascular grafts capable of somatic growth in young lambs, Nat. Commun. 7 (2016) 12951.
[57] Y. Naito, M. Williams-Fritze, D.R. Duncan, S.N. Church, N. Hibino, J.A. Madri, J.D. Humphrey, T. Shinoka, C.K. Breuer, Characterization of the natural history of extracellular matrix production in tissue-engineered vascular grafts during neovessel formation, Cells Tissues Organs 195 (1–2) (2012) 60–72.
[58] T. Fukunishi, C.A. Best, T. Sugiura, T. Shoji, T. Yi, B. Udelsman, D. Ohst, C.S. Ong, H. Zhang, T. Shinoka, C.K. Breuer, J. Johnson, N. Hibino, Tissue-engineered small diameter arterial vascular grafts from cell-free nanofiber PCL/Chitosan scaffolds in a sheep model, PLoS One 11 (7) (2016) e0158555.
[59] G. Matsumura, N. Isayama, S. Matsuda, K. Taki, Y. Sakamoto, Y. Ikada, K. Yamazaki, Long-term results of cell-free biodegradable scaffolds for in situ tissue engineering of pulmonary artery in a canine model, Biomaterials 34 (27) (2013) 6422–6428.
[60] I. Cummings, S. George, J. Kelm, D. Schmidt, M.Y. Emmert, B. Weber, G. Zund, S.P. Hoerstrup, Tissue-engineered vascular graft remodeling in a growing lamb model: expression of matrix metalloproteinases, Eur. J. Cardiothorac. Surg. 41 (1) (2012) 167–172.
[61] S.P. Hoerstrup, I. Cummings Mrcs, M. Lachat, F.J. Schoen, R. Jenni, S. Leschka, S. Neuenschwander, D. Schmidt, A. Mol, C. Gunter, M. Gossi, M. Genoni, G. Zund, Functional growth in tissue-engineered living, vascular grafts: follow-up at 100 weeks in a large animal model, Circulation 114 (1 Suppl) (2006) I159–I166.
[62] G. Kohler, L. Pallwein-Prettner, O.O. Koch, R.R. Luketina, M. Lechner, K. Emmanuel, Magnetic resonance-visible meshes for laparoscopic ventral hernia repair, J. Soc. Laparoendosc. Surg. 19 (1) (2015) e2014 00175.
[63] N.L. Hansen, A. Barabasch, M. Distelmaier, A. Ciritsis, N. Kuehnert, J. Otto, J. Conze, U. Klinge, R.D. Hilgers, C.K. Kuhl, N.A. Kraemer, First in-human magnetic resonance visualization of surgical mesh implants for inguinal hernia treatment, Investig. Radiol. 48 (11) (2013) 770–778.
[64] N.A. Kraemer, H.C. Donker, N. Kuehnert, J. Otto, S. Schrading, G.A. Krombach, U. Klinge, C.K. Kuhl, In vivo visualization of polymer-based mesh implants using conventional magnetic resonance imaging and positive-contrast susceptibility imaging, Investig. Radiol. 48 (4) (2013) 200–205.
[65] N.A. Kramer, H.C. Donker, J. Otto, M. Hodenius, J. Senegas, I. Slabu, U. Klinge, M. Baumann, A. Mullen, B. Obolenski, R.W. Gunther, G.A. Krombach, A concept for magnetic resonance visualization of surgical textile implants, Investig. Radiol. 45 (8) (2010) 477–483.
[66] W.G. Chang, L.E. Niklason, A short discourse on vascular tissue engineering, NPJ Regen Med 2 (2017).
[67] R.D. Kirkton, M. Santiago-Maysonet, J.H. Lawson, W.E. Tente, S.L.M. Dahl, L.E. Niklason, H.L. Prichard, Bioengineered human acellular vessels recellularize and evolve into living blood vessels after human implantation, Sci. Transl. Med. 11 (485) (2019).
[68] Z. Chen, C. Yan, S. Yan, Q. Liu, M. Hou, Y. Xu, R. Guo, Non-invasive monitoring of in vivo hydrogel degradation and cartilage regeneration by multiparametric MR imaging, Theranostics 8 (4) (2018) 1146–1158.
[69] D. Bermejo-Velasco, W. Dou, A. Heerschap, D. Ossipov, J. Hilborn, Injectable hyaluronic acid hydrogels with the capacity for magnetic resonance imaging, Carbohydr. Polym. 197 (2018) 641–648.
[70] M.H. Bakker, C.C.S. Tseng, H.M. Keizer, P.R. Seevinck, H.M. Janssen, F.J. Van Slochteren, S.A.J. Chamuleau, P.Y.W. Dankers, MRI visualization of injectable ureidopyrimidinone hydrogelators by supramolecular contrast agent labeling, Adv. Healthc. Mater. 7 (11) (2018) e1701139.
[71] H.P. Janke, N. Guvener, W. Dou, D.M. Tiemessen, A. YantiSetiasti, J.G.O. Cremers, P.J.A. Borm, W.F.J. Feitz, A. Heerschap, F. Kiessling, E. Oosterwijk, Labeling of collagen type I templates with a naturally derived contrast agent for noninvasive MR imaging in soft tissue engineering, Adv. Healthc. Mater. 7 (18) (2018) e1800605.
[72] T. Lammers, M.E. Mertens, P. Schuster, K. Rahimi, Y. Shi, V. Schulz, A.J.C. Kuehne, S. Jockenhoevel, F. Kiessling, Fluorinated polyurethane scaffolds for (19)F magnetic resonance imaging, Chem. Mater. 29 (7) (2017) 2669–2671.
[73] S.M. Forton, M.T. Latourette, M. Parys, M. Kiupel, D. Shahriari, J.F. Sakamoto, E.M. Shapiro, Vivo microcomputed tomography of nanocrystal-doped tissue engineered scaffolds, ACS Biomater. Sci. Eng. 2 (4) (2016) 508–516.
[74] O. Ogunlade, J.O.Y. Ho, T.L. Kalber, R.E. Hynds, E. Zhang, S.M. Janes, M.A. Birchall, C.R. Butler, P. Beard, Monitoring neovascularization and integration of decellularized human scaffolds using photoacoustic imaging, Photoacoustics 13 (2019) 76–84.